

# Multi-Center Magnon Excitations Open the Entire Brillouin Zone to Terahertz Magnetometry of Quantum Magnets

*Tobias Biesner<sup>†</sup>, Seulki Roh<sup>†</sup>, Aleksandar Razpopov, Jannis Willwater, Stefan Süllow, Ying Li, Katharina M. Zoch, Marisa Medarde, Jürgen Nuss, Denis Gorbunov, Yurii Skourski, Andrej Pustogow, Stuart E. Brown, Cornelius Krellner, Roser Valentí\*, Pascal Puphal\*, Martin Dressel\**

<sup>†</sup>*These authors contributed equally. \*Corresponding author*

T. Biesner, Dr. S. Roh, Ass. Prof. A. Pustogow, Prof. M. Dressel  
1. Physikalisches Institut, Universität Stuttgart, Stuttgart, Germany  
Email Address: dressel@pi1.physik.uni-stuttgart.de (M.D.)

A. Razpopov, Dr. Y. Li, Prof. R. Valentí  
Institut für Theoretische Physik, Goethe-Universität Frankfurt, Frankfurt am Main, Germany  
Email Address: valenti@itp.uni-frankfurt.de (R.V.)

J. Willwater, apl. Prof. S. Süllow  
Institut für Physik der Kondensierten Materie, Technische Universität Braunschweig, Braunschweig, Germany

Dr. Y. Li  
Department of Applied Physics and MOE Key Laboratory for Nonequilibrium Synthesis and Modulation of Condensed Matter, School of Physics, Xi'an Jiaotong University, Xi'an, China

K. M. Zoch, Prof. C. Krellner, Dr. P. Puphal  
Physikalisches Institut, Goethe-Universität Frankfurt, Frankfurt am Main, Germany

Dr. M. Medarde, Dr. P. Puphal  
Laboratory for Multiscale Materials Experiments, Paul Scherrer Institute, 5232 Villigen PSI, Switzerland

Dr. J. Nuss, Dr. P. Puphal  
Max Planck Institute for Solid State Research, Stuttgart, Germany  
Email Address: p.puphal@fkf.mpg.de (P.P.)

Dr. D. Gorbunov, Dr. Y. Skourski  
Hochfeld-Magnetlabor Dresden (HLD-EMFL), Helmholtz-Zentrum Dresden-Rossendorf, 01328 Dresden, Germany

Ass. Prof. A. Pustogow, Prof. S. E. Brown  
Department of Physics and Astronomy, UCLA, Los Angeles, USA

Ass. Prof. A. Pustogow  
Institute of Solid State Physics, TU Wien, 1040 Vienna, Austria

arXiv:2203.04343v1 [cond-mat.str-el] 8 Mar 2022

Keywords: *multi-center magnon, spin density, kagome lattice, terahertz photon, terahertz magnetometry*

Due to the small photon momentum, optical spectroscopy commonly probes magnetic excitations only at the center of the Brillouin zone; however, there are ways to override this restriction. In the case of the distorted kagome quantum magnet Y-kapellasite,  $\text{Y}_3\text{Cu}_9(\text{OH})_{19}\text{Cl}_8$ , under scrutiny here, the magnon density of states can be accessed over the entire Brillouin zone through three-center magnon excitations. This mechanism is aided by the three different magnetic sublattices and strong short-range correlations in the distorted kagome lattice. The results of THz time-domain experiments agree remarkably well with linear spin-wave theory. Relaxing the conventional zone-center constraint of photons gives a new aspect to probe magnetism in matter.

## 1 Introduction

Conservations of momentum and energy are fundamental principles in physics that have to be obeyed also by optical excitations in solids. In an isolated system, for example, direct electronic transitions induced by light follow both  $\Delta E = E_{ph}$  and  $\Delta \mathbf{q} = \mathbf{q}_{ph}$ , where  $\Delta E$  and  $\Delta \mathbf{q}$  are the energy and momentum differences between the initial and the excited states, respectively, while  $E_{ph}$  and  $\mathbf{q}_{ph}$  are energy and momentum of the photon.<sup>[1,2]</sup> By the same token, these two principles dictate magnetic excitations as well. Here, a magnon with momentum  $\mathbf{q}$  is created / annihilated by absorbing / emitting a photon. Within the energy conservation limit, the small photon momentum confines possible excitations close to the center of the Brillouin zone (BZ), i.e.  $\mathbf{q} \approx 0$ , due to its sharp energy-momentum dispersion ( $\omega = q_{ph}c_0/n$ ,  $\omega$ : angular frequency,  $c_0$ : speed of light in vacuum,  $n$ : refractive index of medium). Thus, optical accesses, for instance in Raman and THz spectroscopy, to the magnetic transitions are focused on the zone-center magnons.<sup>[3-8]</sup> On the other hand, neutron scattering covers a broad range in the Brillouin zone due to large momenta of neutrons, promoting this technique as ideal spectroscopic tool to map spin dispersion. In reality, however, the picture is tainted by the low energy and wavevector resolution of neutron scattering experiments and restriction to large-scale facilities. Further constraints arise from the required large sample mass and the preference to avoid hydrogen and other isotopes with strong neutron absorption. In turn, optical techniques could provide easy access to the magnetism albeit the  $\mathbf{q} \approx 0$  constraint. Attempts to overcome this constraint are subject of current research and first promising results have been reported.<sup>[9-11]</sup>

In THz spectroscopy, with the aid of ultrafast lasers and advanced detection schemes, dynamical processes in the (sub-) picosecond range become accessible.<sup>[12,13]</sup> This progress allows not only performing time-resolved studies but enables a control of magnetization dynamics.<sup>[14-16]</sup> Magnetic properties can be probed, for instance, through the magneto-optical Faraday or Kerr effects.<sup>[17,18]</sup> Other examples include the coherent generation of magnons.<sup>[11]</sup> Control over THz-driven spin precession<sup>[19-22]</sup> opens the field of THz magnetometry, i.e. the fully optical extraction of magnetic properties.<sup>[23]</sup>

Here, we demonstrate the potential of THz time-domain spectroscopy (THz-TDS)<sup>[24]</sup> in easing its zone-center restriction: the spin (magnon) density of states (SDOS) can be probed over the entire Brillouin zone via multi-center magnon absorption in materials with several magnetic sublattices. In this picture, magnon excitations take place simultaneously in different magnetic sublattices and positions in momentum space,  $\mathbf{q}_n$ .<sup>[25-27]</sup> Yet, the summed momenta of the participating magnons are zero,  $\sum_n \mathbf{q}_n \approx 0$ , achieving momentum conservation. **Figure 1a** compares the conventional excitation picture, i.e. one-magnon process ( $\mathbf{q} \approx 0$ ), with the multi-center magnon process ( $\Delta \mathbf{q} \approx 0$ ). The distinction between both is prominent in the THz susceptibility  $\chi_m''$  and in the time-dependent electric field of the probing

light. Here, the  $\mathbf{q} \approx 0$  mode (one-magnon) causes a homogeneous precession of spins,<sup>[14,28]</sup> resulting in sharp spectral features in  $\chi_m''$  and relatively long oscillations of the electric field (20-40 ps)<sup>[29,30]</sup> through a free induction decay mechanism.<sup>[19-22]</sup> The multi-center magnon absorption yields a broad feature<sup>[25,31,32]</sup> implying a reduced lifetime (cf. red and yellow contributions in Figure 1a). It can be observed even above the magnetic long-range ordering temperature  $T_N$  as a semblance of paramagnons (paramagnons are observed by various methods, see References<sup>[33-35]</sup>).

We have chosen the quantum magnet<sup>[36-40]</sup> Y-kapellasite ( $\text{Y}_3\text{Cu}_9(\text{OH})_{19}\text{Cl}_8$ )<sup>[41]</sup> as our material platform. Y-kapellasite forms a distorted kagome lattice and has attracted attention recently due to its intriguing magnetic ground state ( $T_N = 2.2$  K), suggested in Figure 1b.<sup>[42]</sup> Here, the magnetic supercell is comprised of three hexagons rotated by  $120^\circ$ . Due to the three possible arrangements, we define each hexagon as a magnetic sublattice and give it one of the colors: green, blue, or yellow. Strong short-range magnetic correlations and persistent spin dynamics below the ordering temperature (down to  $T = 20$  mK) were reported previously.<sup>[41,43]</sup> The THz transmission of Y-kapellasite was measured over a wide temperature and magnetic field range. At low temperatures ( $T < 30$  K), we find magnetically active, continuum-like excitations decaying through oscillations of the transient electric field during an extended time period of around 5 ps. By comparison to the linear spin-wave theory, we conclude that the THz  $\chi_m''$  encodes the SDOS through a multi-center magnon absorption, three-center magnon, augmented by the distinct magnetic ground state of Y-kapellasite, as described in Figure 1b. We propose THz magnetometry via multi-center magnon absorption as a method to overcome the conventional zone-center restriction providing access to magnetism over the entire Brillouin zone.

## 2 Results

### 2.1 Magnetic properties of Y-kapellasite

In Y-kapellasite, a distorted kagome lattice is formed by two distinct Cu sites, as depicted in **Figure 2a**. Here, the magnetic superexchange is governed along three different Cu-O-Cu paths.<sup>[41,42]</sup> The distorted kagome planes stack along the  $c$ -direction (Figure 2b). See supplement for further material information (**Figure S1 and S2**). Let us first consider the static response of the spin system. The in-plane magnetic susceptibility ( $\mathbf{H} \parallel (a, b)$ ) down to temperatures as low as  $T = 400$  mK is presented in Figure 2c. Focusing on the  $H = 0.1$  T measurements, upon cooling, the magnetization first saturates in a plateau at intermediate temperatures ( $T = 50$  K) and continues to rise below  $T = 30$  K. At around  $T = 3$  K a maximum develops, followed by a smaller peak at lower temperature ( $T = 1.5$  K). While the maximum at  $T = 3$  K is consistent with the previously reported  $T_N = 2.2$  K,<sup>[41]</sup> also observed in heat-capacity measurements, the additional smaller peak suggests a successive freezing of the magnetic texture at lower temperatures. This is in accordance with the recent  $\mu$ SR study on polycrystalline samples,<sup>[43]</sup> reporting persistent spin dynamics down to the mK range. Furthermore, a weak hysteresis between field cooled (FC) and zero field cooled (ZFC) measurements is observed below  $T = 3$  K, whereas the cooling protocol does not affect the susceptibility noticeably at higher temperatures, indicating the contribution of uncompensated spins at low temperatures. Increasing the external magnetic field, the magnetization is slightly suppressed and the 3 K-peak shifts to lower temperatures, implying dominant antiferromagnetic interactions. This result suggests two different characteristic temperatures in Y-kapellasite, around  $T = 30$  K and  $T_N = 2.2$  K.

For additional information, the magnetic properties of Y-kapellasite are further investigated using nuclear magnetic resonance (NMR) and electron spin resonance (ESR). Starting with the  $^1\text{H}$ -NMR characterization (Figure 2d), the in-plane spin-lattice relaxation rate  $1/T_1$  first decreases upon cooling and increases again near  $T = 30$  K. This crossover indicates the onset of short-range magnetic correlations. A similar temperature scale is found by ESR measurements as shown in Figure 2d, left axis (**Figure S3** for extended ESR spectra). Simultaneously with the onset of magnetic correlations at around  $T = 30$  K, the electron spin susceptibility  $\chi_s^e$  starts to rise, advocating the close relation between the ESR absorption and the short-range magnetic interactions. Additional measurements, high-field magnetization and ac susceptibility, reveal similar temperature scales and are presented in the supplement (cf. **Figure S4 and S5**). The range between  $T \approx 30$  K (short-range magnetic correlations) and  $T_N \approx 2.2$  K offers experimental access for investigating the emergence of magnetism on the kagome lattice above  $T_N$ , as sketched in Figure 2e. The desired multi-center magnon absorption could survive for higher temperatures through these short-range magnetic correlations.

### 2.2 THz time-domain spectra as a probe of spin dynamics

In **Figure 3** we plot the raw data of the THz-TDS recorded in the  $ab$ -plane. At high temperatures, the in-plane time-domain signal of the transient electric field (Figure 3a) consists of only the main pulse ranging from 0 to 4 ps (see Methods). With cooling, the intensity of this pulse decreases, but in addition a pronounced oscillating electric field develops over an extended time ranging from 4 to 10 ps. Note,

for conventional one-magnon excitations, a similar time-domain signal was reported but on a significantly longer time scale (several tens of ps).<sup>[20–22,29,30]</sup> To gain more insight into the underlying physical processes, we perform a Fourier transformation and calculate the frequency-dependent absorption coefficient  $\alpha$ , plotted in Figure 3b. At room temperature, only the tail of the lowest in-plane phonon mode contributes notably to the THz absorption. Upon cooling, the phonon contribution first increases slightly and then becomes weaker together with a suppression of the main pulse in the time-domain signal (see supplement, **Figure S6** for the results of infrared spectroscopy and DFT calculations of the phonons). As the temperature drops below  $T = 30$  K, we see the low-frequency absorption rising, resulting in a broad continuum-like contribution much stronger than the phonon (in this frequency range). This corresponds to the enhancement of the electric field oscillations at extended times as illustrated in Figure 3a. The feature increases strongly with further cooling and finally dominates the entire THz response down to the lowest temperature measured. Furthermore, for  $T < 5$  K, we observe two weaker, but noticeable, peak-like contributions between  $30 - 40$   $\text{cm}^{-1}$ . Despite the increase of intensity, no qualitative difference can be found in measurements below  $T_N$ . From the comparison with our calculations, we can exclude a phononic origin of the low-energy features. Also electronic contributions are unlikely for the highly insulating Y-kapellasite (bandgap of 3.6 eV).<sup>[41,44]</sup>

These trends become even more obvious when looking at the integrated absorption  $IA$  (similar to the spectral weight, see method section), displayed in the inset of Figure 3b. The crossover range in  $IA(T)$  matches well with the onset of short-range magnetic correlations at around  $T = 30$  K as observed in the NMR spin-lattice relaxation rate and ESR susceptibility. This good agreement between the temperature scales strongly suggests that the THz continuum-like absorption is caused by short-range magnetic correlations even above  $T_N$  (see supplemental **Figure S7** for corresponding spectra covering the entire temperature range; **Figure S8** for additional data in the frequency domain).

### 2.3 Magneto-THz spectroscopy

To clarify the magnetic origin of this continuum-like absorption, we carried out magneto-THz measurements at  $T = 1.7$  K while applying a static magnetic field up to  $H = 10$  T in Faraday geometry. With ramping up the magnetic field, the continuum-like feature loses its intensity beginning at the low-frequency end, as displayed in **Figure 4a** (**Figure S9** for extended data). This can be nicely seen in Figure 4b where the  $IA$  is plotted as a function of  $H$ . Exceeding a critical field of  $H_c = 3$  T,  $IA(H)$  decreases considerably; at a field strength of  $H = 10$  T the intensity is reduced by almost 10 %. This quantitative change seems reasonable since the magnetic energy corresponds to roughly 10 % of the exchange energy:  $\mu_B H = 0.1 k_B \Theta_{CW} \approx 0.1 J$ , where  $\Theta_{CW} \approx -100$  K is the Curie-Weiss temperature and  $J \approx 13$  meV is the dominating exchange energy ( $\mu_B$  is Bohr magneton,  $k_B$  is Boltzmann constant).<sup>[41,42]</sup> The phonon tail above  $40$   $\text{cm}^{-1}$  is affected as well: it weakly shifts towards lower energies. In addition to these obvious changes in the spectrum, we can identify some more subtle variations inside the continuum-like absorption. Slight shifts of the  $30 - 40$   $\text{cm}^{-1}$  peaks become clearer in the contour plot of the normalized absorption coefficient  $\alpha(H)/\alpha(0 \text{ T})$ , presented in Figure 4c. Interestingly, the onset of the continuum-like absorption shows a stronger change under magnetic field, compared to the  $30 - 40$   $\text{cm}^{-1}$  peaks, c.f. grey arrows in Figure 4c. Note the reduced signal-to-noise ratio of a magneto-

optical measurement leads to somewhat noisy features below  $20 \text{ cm}^{-1}$ ; nevertheless, our magneto-optical THz results strongly support the magnetic origin of the continuum-like feature.

## 2.4 Multi-center magnon excitations

In a next step we have to separate the magnetic contributions from the dielectric ones in the THz absorption in order to reveal their natural spectral form. With the fair assumption that the dielectric properties do not change drastically at low temperatures, the magnetic susceptibility  $\chi_m''$  can be obtained from the THz spectra (Figure 3) by referencing to the 80 K-spectrum (see method section for further information). The results are shown in **Figure 5a**. The extraction of  $\chi_m''$  unveils an asymmetric shape of the magnetic continuum-like feature with a maximum at around  $12 \text{ cm}^{-1}$  and a width of about  $30 \text{ cm}^{-1}$  followed by two peaks at  $32$  and  $37 \text{ cm}^{-1}$  at the lowest temperature,  $T = 1.6 \text{ K}$ .

To learn more about the origin of the magnetic THz response and the magnetic ground state, we calculated the spin-wave dispersion for Y-kapellasite with linear spin-wave theory by assuming a coplanar non-collinear  $\mathbf{Q} = (1/3, 1/3)$  magnetically ordered ground state as suggested by recent *ab-initio* DFT calculations.<sup>[42]</sup> This ordered state comprises three different magnetic sublattices of hexagons (shown as green, blue, and yellow in Figure 1b). Within each hexagon, the spins are antiferromagnetically coupled and neighboring hexagons are coupled to each other via spins (shown in grey) whose directions are fully determined by the neighboring hexagons (slave spins).<sup>[42]</sup>

Figure 5b and c contain the calculated spin density of states (SDOS) and the corresponding spin-wave dispersion in the relevant energy range, below  $6 \text{ meV}$  ( $1 \text{ meV}$  corresponds to  $8.065 \text{ cm}^{-1}$ ). Several energies with a density of states, corresponding to characteristic energy scales of the THz  $\chi_m''$ , are marked by dashed lines. The spin-wave dispersion of Y-kapellasite is gapless and degenerated at the  $\Gamma$ -point (Goldstone mode); possible one-magnon excitations are outside our THz spectral range (**Figure S10**). As introduced above, a one-magnon process only measures the response at the zone center; in stark contrast to multi-center magnon excitations that can expand over the entire Brillouin zone. For the latter case, due to momentum conservation, the total wavevector of the participating magnons must be zero,  $\sum_n \mathbf{q}_n \approx 0$ , which is accomplished by the simultaneous magnon excitations in three distinct magnetic sublattices. Within this picture, the steady development of the continuum-like absorption without any additional features across  $T_N$  can be explained by multi-center magnon absorptions. The one-magnon excitations are outside our accessible spectral range and only the multi-center magnons are observed. As illustrated in Figure 5d, the spin-wave dispersion beyond the  $\Gamma$ -point gets accessible via such excitations. Indeed, towards the K-direction the degeneracy is lifted and the lowest band exhibits a parabolic shape (Figure 5c). Around  $2.7 \text{ meV}$  the band flattens and reaches a maximum. This shape of the dispersion yields a large number of available states in the low-energy range and generates the maximum in the SDOS at  $2.7 \text{ meV}$  which is related to the peak at  $1.5 \text{ meV}$  ( $12 \text{ cm}^{-1}$ ) in  $\chi_m''$ . At higher energies, around  $4.8 \text{ meV}$ , the density of states increases again with the next two higher-lying bands reaching their maxima. At  $5 \text{ meV}$  the number of available states drops significantly before it peaks again at around  $5.2 \text{ meV}$  (parabola minima of the next higher bands). Indeed, these states are related to the peak-like contributions between  $32$  and  $37 \text{ cm}^{-1}$  ( $4$  and  $4.6 \text{ meV}$ ) in  $\chi_m''$  (Figure 5a). There is a small offset of about  $1 \text{ meV}$  between experimental results and calculations, probably due to a small mismatch

in parameters between experiment and theory.

Overall, including the multi-center magnon picture, the SDOS from the linear spin-wave calculations show a remarkable agreement with the experimental result,  $\chi_m''$ . Furthermore, based on the SDOS, we calculated the expected  $\chi_m''$ , validating the observed spectral shape (cf. **Figure S11**). The agreement with theory even extends to the magnetic field dependence. Figure 5b displays the change of the SDOS with magnetic field. Under external magnetic field, the spin dispersion becomes gapped and the weight of the SDOS shifts up in energy (**Figure S12 and S13**). In addition, the 2.7 meV maximum reveals a strong shift under magnetic field, it is slightly different than the one obtained for the 4.8 meV and 5.2 meV peaks. We note that the calculations overestimate the magnetic field scale compared to that of the experiment, perhaps due to demagnetization effects. Still, these trends under external magnetic field are corroborating the result of our magneto-THz spectroscopy, displayed in Figure 4.

### 3 Discussion

Our THz study allows to directly probe the spin density of states via optical spectroscopy; by utilizing multi-center magnon absorption we gain access to the SDOS over the entire Brillouin zone, i.e. we actually perform THz magnetometry. In Y-kapellasite, strong short-range magnetic correlations lead to spin fluctuations over a wide temperature range. The paramagnonic behavior is aided by these fluctuations explaining the development of the THz continuum-like absorption together with the onset of short-range magnetic correlations. The lattice distortion, on the other hand, lowers the spatial symmetry and generates three magnetic sublattices. This distortion is decisive for multi-center magnon excitations to occur. In particular, the magnetic superstructure favors simultaneous  $3N$  magnon excitations where each of the participating magnon excitations occurs, respectively, at one of the three magnetic sublattices, i.e. three-center magnon, while in total the net momentum is conserved ( $\Delta\mathbf{q} = \mathbf{q}_{ph} \approx 0$ ), as illustrated in Figure 1b (see supplement for further discussion, **Figure S14**). We suggest that the role of distortion could be further verified in other kagome lattices.<sup>[42,45-47]</sup> But for the case of Y-kapellasite, the distortion seems to be crucial for the multi-center magnon absorption given that Herbertsmithite, which is considered as a perfect kagome structure,<sup>[39]</sup> does not reveal any signature of multi-center magnons (**Figure S15**).<sup>[48,49]</sup>

Such a symmetry breaking can also be phonon-assisted.<sup>[50,51]</sup> We note that similar suggestions were made for the parent compound of cuprates with an underlying square lattice. In those cases, the observed features were associated with the coupling between magnons and phonons leading to enhanced excitation frequencies in the mid-infrared range.<sup>[52,53]</sup> The magneto-elastic coupling may be represented in the temperature dependence of the phonon modes. In the present case, we observe unusual redshifts and anomalies of the infrared-active phonons accompanied by the development of short-range magnetic correlations (Figure S6).

Overall, the comparison of our experimental results with linear spin-wave calculations suggests that for a proper description a multi-center magnon picture is required: we have to go beyond a simple magnetic mode in order to explain the THz excitations. In fact, the multi-center magnon absorption in Y-kapellasite resembles the conventional two-center magnon absorption observed in classical antiferromagnets:  $\text{FeF}_2$ ,  $\text{MnF}_2$ ,  $\text{CoF}_2$ , and  $\text{NiF}_2$ .<sup>[25,27,31,54-57]</sup> Utilizing Dexter's theory of cooperative optical absorption,<sup>[58]</sup> earlier reports proposed several mechanisms,<sup>[54,55,59]</sup> where the removal of centrosymmetric points is supposed to be particularly necessary for the non-vanishing electric dipole moment.<sup>[27]</sup>

The former studies confined the two-center magnon absorption as electric dipole active phenomena; but there is no reason for this limitation. Recently, a direct coupling between the magnetic state and light was proposed; the detection takes place over the free induction decay.<sup>[19-22]</sup> As well, accounting for the two magnetic sublattices in conventional antiferromagnets, traditionally only a two-center absorption was considered. Moreover, the optical selection rule for the three-center magnon excitation might differ from the conventional one-magnon picture ( $\Delta S = \pm 1$ , the spin difference between initial and excited state). For example, the two-center magnon excitation was discussed before with an altered optical selection rule.<sup>[60,61]</sup> All these now turn into limiting factors when a more detailed and generalized microscopic picture has to be established for the multi-center magnon absorption. Together with a refined un-



derstanding, our approach might be applicable in a large pool of materials.

We further discuss the relation of the THz multi-center magnon absorption to similar multimagnon processes observed in other quantum magnets of low symmetry. For quantum magnets, often a virtual process via the magnon decay<sup>[62]</sup> is discussed, which has been observed in Raman/ neutron scattering.<sup>[63–66]</sup> Note that multimagnon scattering (photon/ neutron scatters by creating multiple magnons) and THz multi-center magnon absorption (multi-center magnon: one photon gets absorbed, simultaneously creating multiple magnons in different magnetic sublattices) need to be discerned with distinct optical selection rules.<sup>[27]</sup> Moreover, the higher-order magnon contributions beyond linear spin-wave theory are as well discussed in THz absorption.<sup>[67]</sup> However, these are different from the multi-center magnon absorption, subject of our study. Regarding higher-order magnons, mixing of one-magnon branches with multimagnon states can occur as a result of the low symmetry of the spin interactions as in  $\alpha$ -RuCl<sub>3</sub>.<sup>[68,69]</sup> A further example can be found in the case of Yb<sub>2</sub>Ti<sub>2</sub>O<sub>7</sub>, showing a field-induced decay of the one-magnon branch into a two-magnon continuum.<sup>[63]</sup> In Y-kapellasite, however, neither geometrical frustration nor anisotropic spin interactions seem to be present in the system<sup>[42]</sup> excluding the magnon decay processes from the present case. Nevertheless, we note that a multi-center magnon based extraction of the SDOS with THz spectroscopy, as presented in this work, might be possible even in the presence of a decay mechanism.

There are several issues concerning the magnetic properties of Y-kapellasite which should be addressed in future investigations. One particularly interesting issue remaining is the persistent spin dynamics in the magnetically ordered state below  $T_N = 2.2$  K<sup>[43]</sup> which might be related to the successive spin freezing observed in the susceptibility, Figure 2c. For optical measurements, such a low temperature (mK range) is still challenging. Hence, complementary experimental techniques are required to scrutinize this exotic behavior. In addition, an investigation of the microscopic origin of the short-range magnetic correlations much above  $T_N$  could be a focus of further studies.

---

## 4 Conclusion

In conclusion, in our proof-of-principle experiment, we establish THz time-domain spectroscopy as a method to directly probe the spin density of states expanding its capability from  $\mathbf{q} \approx 0$  to  $\Delta\mathbf{q} \approx 0$  excitations over the entire Brillouin zone: THz magnetometry. The three-center magnon absorption in the exotic magnetic superstructure of Y-kapellasite is the key mechanism behind this observation. Driven by short-range magnetic interactions, the absorption persists well above the magnetic ordering temperature, i.e. we do observe paramagnons. The multi-center magnon absorption allows easy access to the spin density of states for suitable magnets, in particular in systems with low symmetry.

## 5 Experimental Section

*Crystal growth and characterization:* Crystals were grown via a horizontal external gradient growth method. This optimized synthesis leads to nearly perfect defect-free single crystals with large facets (kagome-planes between 2 and 3 mm and thickness of around 0.5-1 mm), see supplement, Figure S1. The results of X-ray diffraction is presented in Figure S2. The ac and dc magnetic susceptibilities were measured as explained in the supplement.

*THz-TDS measurements:* THz time-domain spectroscopy (THz-TDS) measures the time-dependent electric field.<sup>[24]</sup> Through a Fast Fourier Transformation (FFT), intensity and phase can be obtained. This allows us to directly calculate the optical response functions.<sup>[1,2]</sup> A typical time-trace of the transient electric field shows an oscillating behavior with a strong pulse at early times (main pulse). Due to their short lifetime, electronic transitions or phononic resonances are, in general, contained in the main pulse. However, phenomena with a longer lifetime, such as magnetic resonances, can extend to longer times (over several tens of ps), exceeding the main pulse.<sup>[20-22,29,30]</sup>

THz-TDS measurements were carried out in transmission geometry on oriented single crystals ( $\mathbf{E}_{THz} \parallel (a, b)$ ) at several temperatures between 295 and 1.6 K with a helium bath cryostat. Magneto-optical THz measurements were performed in Faraday geometry ( $\mathbf{E}_{THz} \parallel (a, b)$ ,  $\mathbf{H} \parallel c$ ) with static magnetic field strengths up to  $H = 10$  T and temperatures down to 1.7 K. The absorption coefficient  $\alpha$  was calculated from the transmittance  $Tr$  by  $\alpha = -\ln\{Tr\}/d$ , where  $d$  is the sample thickness. The integrated absorption coefficient  $IA = \int \alpha d\omega$  resembles the optical spectral weight and provides a quantitative access to the spectral features (see supplement for further information). The frequency-dependent magnetic susceptibility  $\chi_m'' = \text{Im}\{\tilde{\chi}_m(\omega)\}$  was calculated by referencing to the high-temperature dielectric response,<sup>[5,7,8,70]</sup> i.e. the  $T = 80$  K spectrum, see supplement for further information. This quantity encodes the SDOS, as previously shown for the  $\mathbf{q} \approx 0$  case.<sup>[5]</sup>

*ESR measurements:* Temperature-dependent electron spin resonance (ESR) measurements in the X-band frequency were carried out. The in-plane response was determined with a microwave field  $\mathbf{h} \parallel c$  and external magnetic field  $\mathbf{H} \parallel (a, b)$ . More details are discussed in the supplement.

*NMR characterization:* Nuclear magnetic resonance ( $^1\text{H-NMR}$ ) experiments were performed on a  $3 \times 3 \times 1$  mm<sup>3</sup> sized Y-kapellasite single crystal with magnetic field ( $H = 0.98$  T) aligned parallel to the kagome layers ( $\mathbf{H} \parallel (a, b)$ ). The spin-lattice relaxation rate  $1/T_1$  was measured by non-selective excitation of the full line.  $1/T_1$  was determined through saturation-recovery using single-exponential fits. Temperature control in the range from 4 to 200 K was achieved using a  $^4\text{He}$  cryostat with a variable-temperature insert.

*High-field magnetization:* The high-field magnetization was determined between  $T = 0.5$  and 30 K in pulsed magnetic fields up to 55 T for in-plane and out-of-plane orientations. Further information can be found in the supplement. Measurements were performed at the high field laboratory in Dresden, Germany (HLD-EMFL).

*DFT and LSWT calculations:* The phonon frequencies were calculated using a combination of the PHONOPY package<sup>[71,72]</sup> and Density Functional Theory (DFT) as implemented in the Vienna Ab-

---

Initio Simulation Package (VASP) code.<sup>[73–75]</sup> The details of the calculations are in the supplemental material. The magnon dispersion was determined by using linear spin-wave theory (LSWT) as implemented in SpinW 3.0.<sup>[76]</sup> The details are explained in the supplement.

## Supporting Information

Supporting Information is available from the Wiley Online Library or from the author.

## Acknowledgements

We thank Artem Pronin, Guratinder Kaur, and Reinhard K. Kremer for fruitful discussion, Björn Miksch and Lena N. Majer for help with the ESR measurements and Gabriele Untereiner for continuous technical support. The project was supported by the HLD-HZDR, member of the European Magnetic Field Laboratory (EMFL), and the Deutsche Forschungsgemeinschaft (DFG). A.R. and R.V. thank the DFG through TRR 288-422213477 (project A05). Y.L. acknowledges support by China Postdoctoral Science Foundation (Grant No. 2019M660249) and National Natural Science Foundation of China (Grant No. 12004296). M.M. acknowledges the Swiss National Science Foundation (Grant No. 206021\_139082). A.P. acknowledges support by the Alexander von Humboldt Foundation through the Feodor Lynen Fellowship. The work at University of California, Los Angeles, was supported by NSF Grant 2004553.

## Author contributions

These authors contributed equally: T.B. and S.R.

T.B., S.R. performed the spectroscopic measurements and analyzed the data. P.P., K.M.Z, C.K. grew the crystals. P.P., J.W., S.S., D.G., Y.S., M.M. performed the magnetic characterization. J.N. performed the structural characterization. A.P., S.E.B did the NMR measurements. A.R. performed the LSDW analysis. Y.L. calculated the phonon dispersion. A.P. contributed to the infrared measurements. T.B., S.R., P.P. wrote the manuscript with input from all authors. P.P., T.B., S.R. initiated the project. M.D. and R.V. supervised the project.

## Competing Interests

The authors declare that they have no competing financial interests.

## Correspondence

Correspondence and requests for materials should be addressed to

M.D. (dressel@pi1.physik.uni-stuttgart.de),

P.P. (p.puphal@fkf.mpg.de) or R.V. (valenti@itp.uni-frankfurt.de).

## References

- [1] M. Dressel, G. Grüner, *Electrodynamics of Solids: Optical Properties of Electrons in Matter*, Cambridge University Press, Cambridge, **2002**.
- [2] D. B. Tanner, *Optical Effects in Solids*, Cambridge University Press, Cambridge, **2019**.
- [3] R. S. Fishman, J. A. Fernandez-Baca, T. Rõöm, *Spin-Wave Theory and its Applications to Neutron Scattering and THz Spectroscopy*, Morgan & Claypool Publishers, San Rafael, **2018**.
- [4] D. Wulferding, Y. Choi, W. Lee, K.-Y. Choi, *J. Condens. Matter Phys.* **2019**, *32*, 4 043001.
- [5] X. Zhang, F. Mahmood, M. Daum, Z. Dun, J. A. M. Paddison, N. J. Laurita, T. Hong, H. Zhou, N. P. Armitage, M. Mourigal, *Phys. Rev. X* **2018**, *8* 031001.
- [6] A. Little, L. Wu, P. Lampen-Kelley, A. Banerjee, S. Patankar, D. Rees, C. A. Bridges, J.-Q. Yan, D. Mandrus, S. E. Nagler, J. Orenstein, *Phys. Rev. Lett.* **2017**, *119* 227201.
- [7] P. Chauhan, F. Mahmood, H. J. Changlani, S. M. Koohpayeh, N. P. Armitage, *Phys. Rev. Lett.* **2020**, *124*, 037203.
- [8] N. J. Laurita, J. Deisenhofer, L. Pan, C. M. Morris, M. Schmidt, M. Johnsson, V. Tsurkan, A. Loidl, N. P. Armitage, *Phys. Rev. Lett.* **2015**, *114* 207201.
- [9] T. M. H. Nguyen, L. J. Sandilands, C. H. Sohn, C. H. Kim, A. L. Wysocki, I.-S. Yang, S. J. Moon, J.-H. Ko, J. Yamaura, Z. Hiroi, T. W. Noh, *Nat. Commun.* **2017**, *8*, 1 251.
- [10] L. Wu, A. Little, E. E. Aldape, D. Rees, E. Thewalt, P. Lampen-Kelley, A. Banerjee, C. A. Bridges, J.-Q. Yan, D. Boone, S. Patankar, D. Goldhaber-Gordon, D. Mandrus, S. E. Nagler, E. Altman, J. Orenstein, *Phys. Rev. B* **2018**, *98* 094425.
- [11] J. R. Hortensius, D. Afanasiev, M. Matthiesen, R. Leenders, R. Citro, A. V. Kimel, R. V. Mikhaylovskiy, B. A. Ivanov, A. D. Caviglia, *Nat. Phys.* **2021**, *17*, 9 1001.
- [12] J. Walowski, M. Münzenberg, *J. Appl. Phys.* **2016**, *120*, 14 140901.
- [13] A. Eschenlohr, U. Bovensiepen, *J. Condens. Matter Phys.* **2017**, *30*, 3 030301.
- [14] P. Němec, M. Fiebig, T. Kampfrath, A. V. Kimel, *Nat. Phys.* **2018**, *14*, 3 229.
- [15] T. Kampfrath, K. Tanaka, K. A. Nelson, *Nat. Photonics* **2013**, *7*, 9 680.
- [16] A. V. Kimel, A. Kirilyuk, P. A. Usachev, R. V. Pisarev, A. M. Balbashov, Th. Rasing, *Nature* **2005**, *435*, 7042 655.
- [17] T. Kampfrath, A. Sell, G. Klatt, A. Pashkin, S. Mährlein, T. Dekorsy, M. Wolf, M. Fiebig, A. Leitenstorfer, R. Huber, *Nat. Photonics* **2011**, *5*, 1 31.
- [18] C. Vicario, C. Ruchert, F. Ardana-Lamas, P. M. Derlet, B. Tudu, J. Luning, C. P. Hauri, *Nat. Photonics* **2013**, *7*, 9 720.

- [19] F. Hansteen, A. Kimel, A. Kirilyuk, T. Rasing, *Phys. Rev. Lett.* **2005**, *95* 047402.
- [20] M. Nakajima, A. Namai, S. Ohkoshi, T. Suemoto, *Opt. Express* **2010**, *18*, 17 18260.
- [21] K. Yamaguchi, M. Nakajima, T. Suemoto, *Phys. Rev. Lett.* **2010**, *105* 237201.
- [22] K. Yamaguchi, T. Kurihara, Y. Minami, M. Nakajima, T. Suemoto, *Phys. Rev. Lett.* **2013**, *110* 137204.
- [23] W. Zhang, P. Maldonado, Z. Jin, T. S. Seifert, J. Arabski, G. Schmerber, E. Beaurepaire, M. Bonn, T. Kampfrath, P. M. Oppeneer, D. Turchinovich, *Nat. Commun.* **2020**, *11*, 1 4247.
- [24] J. Neu, C. A. Schmuttenmaer, *J. Appl. Phys.* **2018**, *124*, 23 231101.
- [25] G. B. Wright, editor, *Light Scattering Spectra of Solids*, Springer Berlin Heidelberg, Berlin, Heidelberg, **1969**.
- [26] P. A. Fleury, R. Loudon, *Phys. Rev.* **1968**, *166* 514.
- [27] R. Loudon, *Adv. Phys.* **1968**, *17*, 66 243.
- [28] S. M. Rezende, A. Azevedo, R. L. Rodríguez-Suárez, *J. Appl. Phys.* **2019**, *126*, 15 151101.
- [29] K. Grishunin, T. Huisman, G. Li, E. Mishina, T. Rasing, A. V. Kimel, K. Zhang, Z. Jin, S. Cao, W. Ren, G.-H. Ma, R. V. Mikhaylovskiy, *ACS Photonics* **2018**, *5*, 4 1375.
- [30] J. Lu, X. Li, H. Y. Hwang, B. K. Ofori-Okai, T. Kurihara, T. Suemoto, K. A. Nelson, *Phys. Rev. Lett.* **2017**, *118* 207204.
- [31] M. F. Thorpe, *J. Appl. Phys.* **1970**, *41*, 3 892.
- [32] S. Azuma, M. Sato, Y. Fujimaki, S. Uchida, Y. Tanabe, E. Hanamura, *Phys. Rev. B* **2005**, *71* 014429.
- [33] M. Le Tacon, G. Ghiringhelli, J. Chaloupka, M. Moretti Sala, V. Hinkov, M. W. Haverkort, M. Minola, M. Bakr, K. J. Zhou, S. Blanco-Canosa, C. Monney, Y. T. Song, G. L. Sun, C. T. Lin, G. M. De Luca, M. Salluzzo, G. Khaliullin, T. Schmitt, L. Braicovich, B. Keimer, *Nat. Phys.* **2011**, *7*, 9 725.
- [34] H. J. Qin, Kh. Zakeri, A. Ernst, J. Kirschner, *Phys. Rev. Lett.* **2017**, *118* 127203.
- [35] C. Kadlec, V. Goian, K. Z. Rushchanskii, P. Kužel, M. Ležaić, K. Kohn, R. V. Pisarev, S. Kamba, *Phys. Rev. B* **2011**, *84* 174120.
- [36] L. Balents, *Nature* **2010**, *464*, 7286 199.
- [37] P. Mendels, F. Bert, *C. R. Phys.* **2016**, *17*, 3 455.
- [38] Y. Kohama, H. Ishikawa, A. Matsuo, K. Kindo, N. Shannon, Z. Hiroi, *Proc. Natl. Acad. Sci. U.S.A.* **2019**, *116*, 22 10686.
- [39] M. R. Norman, *Rev. Mod. Phys.* **2016**, *88* 041002.

- [40] J. Knolle, R. Moessner, *Annu. Rev. Condens. Matter Phys.* **2019**, *10*, 1 451.
- [41] P. Puphal, M. Bolte, D. Sheptyakov, A. Pustogow, K. Kliemt, M. Dressel, M. Baenitz, C. Krellner, *J. Mater. Chem. C* **2017**, *5* 2629.
- [42] M. Hering, F. Ferrari, A. Razpopov, I. I. Mazin, R. Valentí, H. O. Jeschke, J. Reuther, *Npj Comput. Mater.* **2022**, *8*, 1 10.
- [43] Q. Barthélemy, P. Puphal, K. M. Zoch, C. Krellner, H. Luetkens, C. Baines, D. Sheptyakov, E. Kermarrec, P. Mendels, F. Bert, *Phys. Rev. Mater.* **2019**, *3* 074401.
- [44] A. Pustogow, Y. Li, I. Voloshenko, P. Puphal, C. Krellner, I. I. Mazin, M. Dressel, R. Valentí, *Phys. Rev. B* **2017**, *96* 241114.
- [45] D. Watanabe, K. Sugii, M. Shimozawa, Y. Suzuki, T. Yajima, H. Ishikawa, Z. Hiroi, T. Shibauchi, Y. Matsuda, M. Yamashita, *Proc. Natl. Acad. Sci. U.S.A.* **2016**, *113*, 31 8653.
- [46] H. Ishikawa, D. Nishio-Hamane, A. Miyake, M. Tokunaga, A. Matsuo, K. Kindo, Z. Hiroi, *Phys. Rev. Mater.* **2019**, *3* 064414.
- [47] D. Boldrin, B. Fåk, E. Canévet, J. Ollivier, H. C. Walker, P. Manuel, D. D. Khalyavin, A. S. Wills, *Phys. Rev. Lett.* **2018**, *121* 107203.
- [48] D. V. Pilon, C. H. Lui, T.-H. Han, D. Shrekenhamer, A. J. Frenzel, W. J. Padilla, Y. S. Lee, N. Gedik, *Phys. Rev. Lett.* **2013**, *111* 127401.
- [49] A. C. Potter, T. Senthil, P. A. Lee, *Phys. Rev. B* **2013**, *87* 245106.
- [50] M. Windt, M. Grüninger, T. Nunner, C. Knetter, K. P. Schmidt, G. S. Uhrig, T. Kopp, A. Freimuth, U. Ammerahl, B. Büchner, A. Revcolevschi, *Phys. Rev. Lett.* **2001**, *87* 127002.
- [51] M. Grüninger, D. van der Marel, A. Damascelli, A. Erb, T. Nunner, T. Kopp, *Phys. Rev. B* **2000**, *62* 12422.
- [52] J. Lorenzana, G. A. Sawatzky, *Phys. Rev. Lett.* **1995**, *74* 1867.
- [53] J. D. Perkins, J. M. Graybeal, M. A. Kastner, R. J. Birgeneau, J. P. Falck, M. Greven, *Phys. Rev. Lett.* **1993**, *71* 1621.
- [54] J. W. Halley, I. Silvera, *Phys. Rev. Lett.* **1965**, *15* 654.
- [55] Y. Tanabe, T. Moriya, S. Sugano, *Phys. Rev. Lett.* **1965**, *15* 1023.
- [56] S. J. Allen, R. Loudon, P. L. Richards, *Phys. Rev. Lett.* **1966**, *16* 463.
- [57] M. F. Thorpe, R. J. Elliott, In G. B. Wright, editor, *Light Scattering Spectra of Solids*, chapter C-2, 199–206. Springer Berlin Heidelberg, Berlin, Heidelberg, **1969**.
- [58] D. L. Dexter, *Phys. Rev.* **1962**, *126* 1962.
- [59] J. W. Halley, *Phys. Rev.* **1967**, *154* 458.



- [60] L. L. Lohr, *Coord. Chem. Rev.* **1972**, *8*, 3 241.
- [61] Y. Tanabe, E. Hanamura, *J. Phys. Soc. Japan* **2005**, *74*, 2 670.
- [62] M. E. Zhitomirsky, A. L. Chernyshev, *Rev. Mod. Phys.* **2013**, *85* 219.
- [63] J. D. Thompson, P. A. McClarty, D. Prabhakaran, I. Cabrera, T. Guidi, R. Coldea, *Phys. Rev. Lett.* **2017**, *119* 057203.
- [64] T. Hong, Y. Qiu, M. Matsumoto, D. A. Tennant, K. Coester, K. P. Schmidt, F. F. Awwadi, M. M. Turnbull, H. Agrawal, A. L. Chernyshev, *Nat. Commun.* **2017**, *8*, 1 15148.
- [65] D. Wulferding, Y. Choi, S.-H. Do, C. H. Lee, P. Lemmens, C. Faugeras, Y. Gallais, K.-Y. Choi, *Nat. Commun.* **2020**, *11*, 1 1603.
- [66] A. Sahasrabudhe, D. A. S. Kaib, S. Reschke, R. German, T. C. Koethe, J. Buhot, D. Kamenskyi, C. Hickey, P. Becker, V. Tsurkan, A. Loidl, S. H. Do, K. Y. Choi, M. Grüninger, S. M. Winter, Z. Wang, R. Valentí, P. H. M. van Loosdrecht, *Phys. Rev. B* **2020**, *101* 140410.
- [67] L. Pan, S. K. Kim, A. Ghosh, C. M. Morris, K. A. Ross, E. Kermarrec, B. D. Gaulin, S. M. Koochpayeh, O. Tchernyshyov, N. P. Armitage, *Nat. Commun.* **2014**, *5*, 1 4970.
- [68] S. M. Winter, K. Riedl, P. A. Maksimov, A. L. Chernyshev, A. Honecker, R. Valentí, *Nat. Commun.* **2017**, *8*, 1 1152.
- [69] Z. Wang, S. Reschke, D. Hüvonen, S.-H. Do, K.-Y. Choi, M. Gensch, U. Nagel, T. Rõõm, A. Loidl, *Phys. Rev. Lett.* **2017**, *119* 227202.
- [70] K. Kozuki, T. Nagashima, M. Hangyo, *Opt. Express* **2011**, *19*, 25 24950.
- [71] A. Togo, F. Oba, I. Tanaka, *Phys. Rev. B* **2008**, *78* 134106.
- [72] A. Togo, I. Tanaka, *Scr. Mater.* **2015**, *108* 1.
- [73] G. Kresse, J. Hafner, *Phys. Rev. B* **1993**, *47* 558.
- [74] G. Kresse, J. Furthmüller, *Phys. Rev. B* **1996**, *54* 11169.
- [75] G. Kresse, J. Furthmüller, *Comput. Mater. Sci.* **1996**, *6*, 1 15.
- [76] S. Toth, B. Lake, *J. Condens. Matter Phys.* **2015**, *27*, 16 166002.

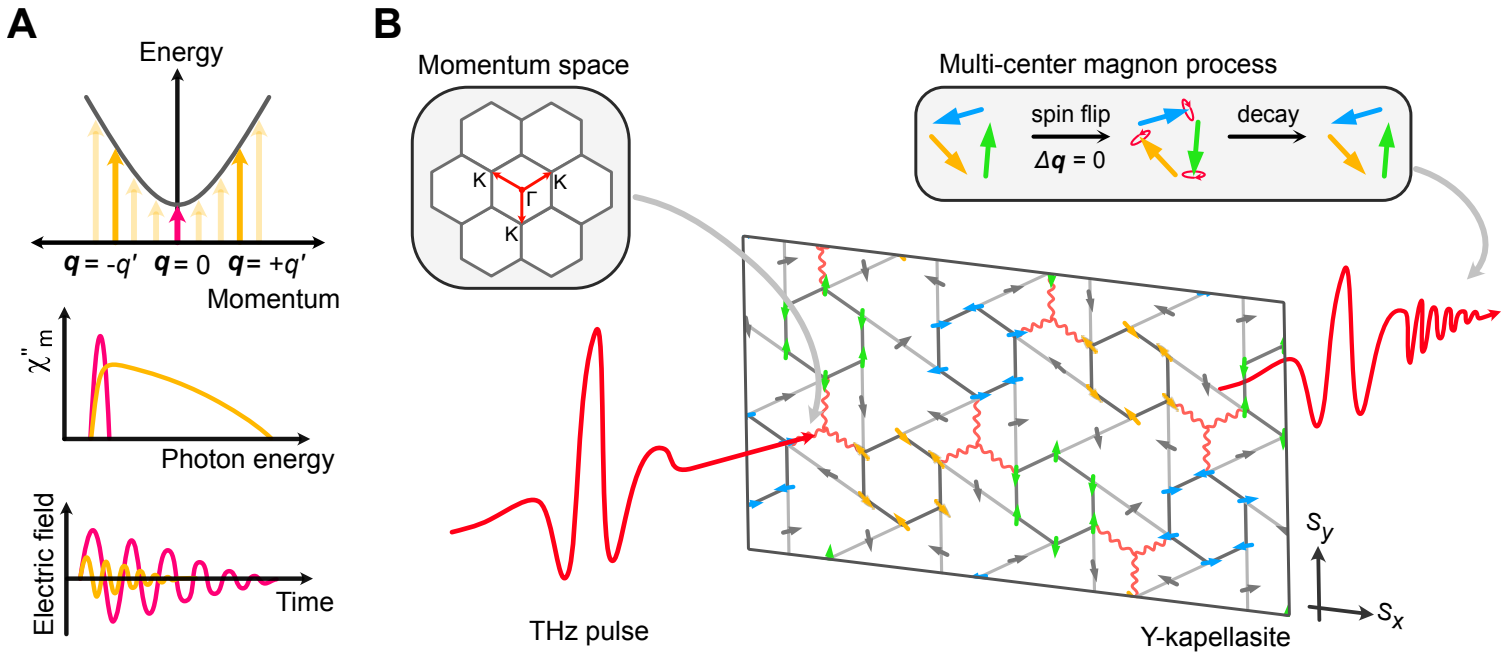


**Figure 1.** Three-center magnon process in Y-kapellasite. a) Comparison between the one-magnon (red) and two-center magnon absorption (yellow). The top panel describes the excitations in the spin dispersion curve. While the one-magnon excitation only takes place near the zone center ( $q \approx 0$ ), the two-center magnon excitations can extend over the entire Brillouin zone ( $\Delta q \approx 0$  excitation). Here, the summed momenta of the participating magnons need to vanish,  $0 \approx \sum_n q_n$ , to ensure momentum conservation. The middle and bottom panel show the corresponding response in energy / frequency-dependent magnetic susceptibility  $\chi''_m$  and electric field as a function of time, respectively. A one-magnon excitation shows a sharp peak in  $\chi''_m$ , due to comparably long lifetimes (20-40 ps). A multi-center magnon process, however, is restricted to shorter time scales, correlated with a broad, continuum-like feature in  $\chi''_m$ . b) Schematics of three-center magnon absorption in Y-kapellasite and calculated ground state,  $\mathbf{Q} = (1/3, 1/3)$ . The simultaneous magnetic absorption occurs through three different magnetic sublattices (green, blue, and yellow hexagons in real space). The excited spin waves fall back to the initial state via a free induction decay resulting in oscillations of the outgoing THz pulse at extended time.

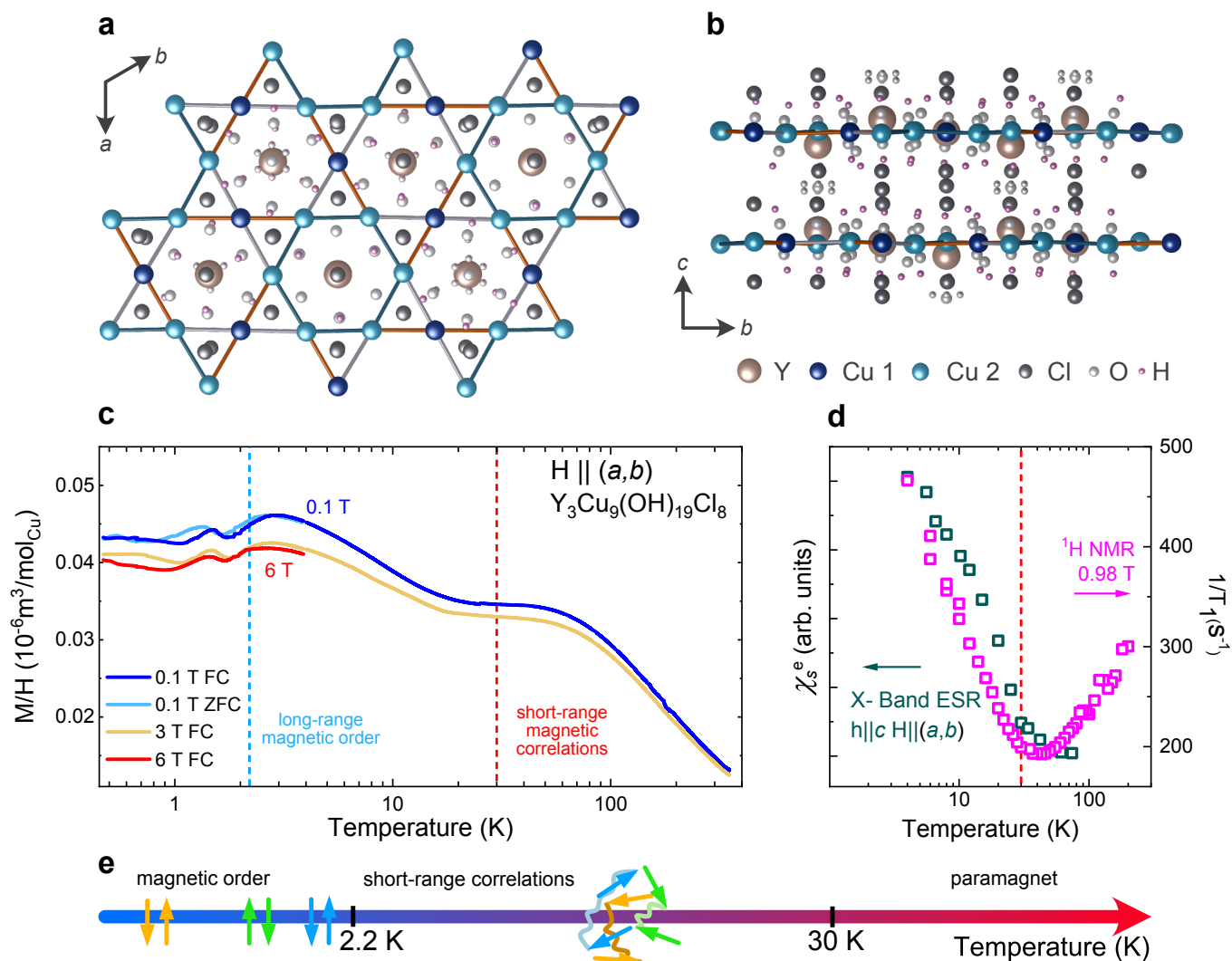


**Figure 2.** Crystal structure and magnetic properties of Y-kapellasite. a) In-plane,  $(a, b)$ -direction and b) out-of-plane ( $c$ -axis) crystal structure. Different copper sites, inducing the distorted kagome bonds (blue, red, grey) are depicted in cyan and dark blue. c) Temperature-dependent dc magnetic susceptibility  $M/H$  (FC - field cooled, ZFC - zero field cooled), under several in-plane magnetic fields. The red dashed line correspond to the onset of short-range magnetic correlations, the light blue dashed line indicates the onset of long-range magnetic order. d) Spin-lattice relaxation rate  $1/T_1$  ( $^1\text{H}$  NMR, right axis) and electron spin susceptibility  $\chi_s^e$  (ESR, left axis). Red dashed line: Onset of short-range magnetic correlations. e) Extracted temperature ranges, onset of short-range magnetic correlations (30 K) and long-range magnetic order (below 2.2 K).

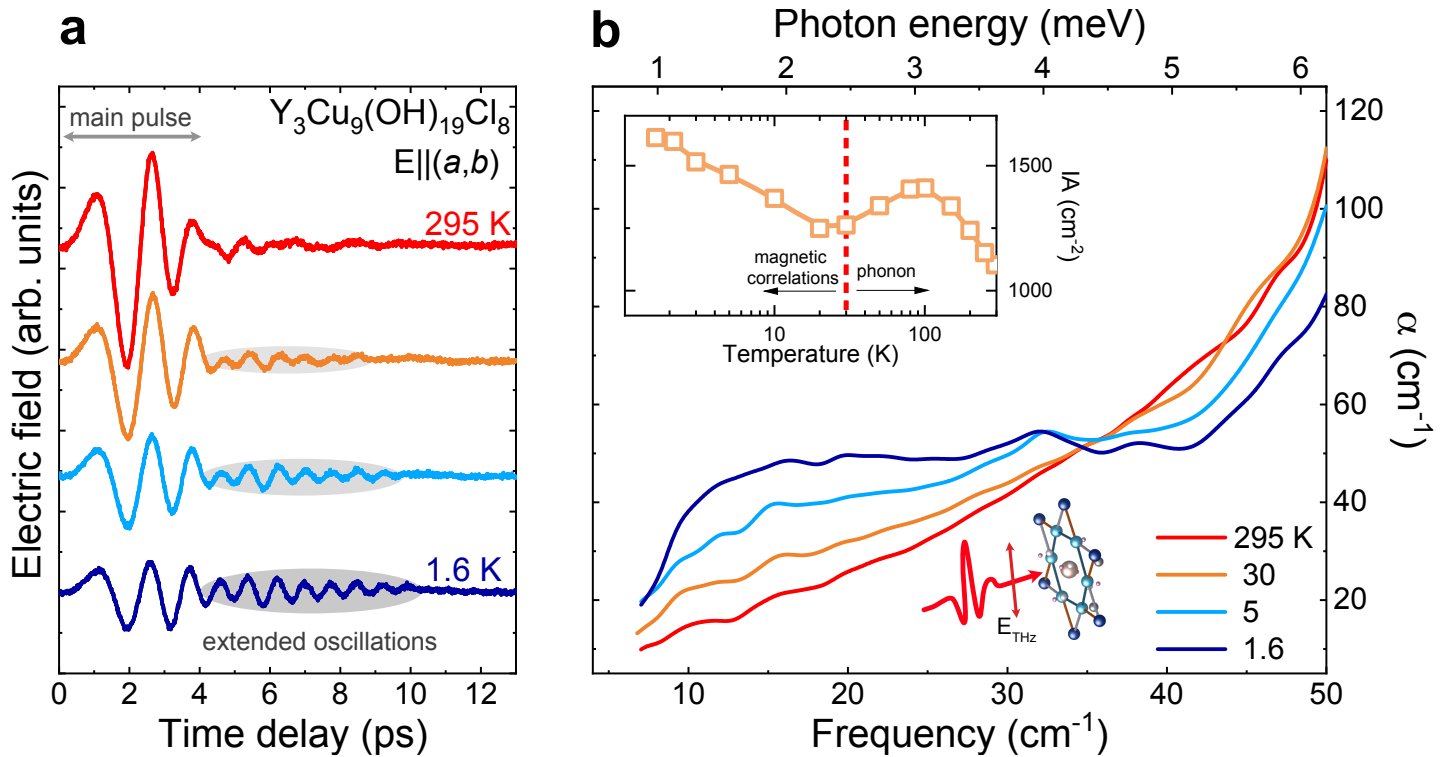


**Figure 3.** Temperature-dependent THz spectra. a) THz electric field, transmitted through Y-kapellasite as a function of time delay and b) resulting absorption coefficient  $\alpha$  for the in-plane direction, as depicted ( $\mathbf{E}_{THz} \parallel (a, b)$ ). At  $T = 295$  K, the main pulse (0 to 4 ps) contains most of the THz responses (phononic properties). Below the onset of short-range magnetic correlations,  $T = 30$  K, the THz electric field pronounces extended-time oscillations (4 to 10 ps, shaded area), while the main pulse loses its intensity. As a result the continuum-like absorption develops in  $\alpha$ , followed by two additional peak-like features at 32 and 37  $cm^{-1}$ . Inset: Integrated absorption coefficient  $IA$  (up to 40  $cm^{-1}$ ). The red dashed line represent the onset of short-range magnetic correlations,  $T = 30$  K. Above  $T = 30$  K, changes in  $IA$  are mostly caused by the lowest in-plane phonon mode. Below the onset of short-range magnetic correlations, the  $IA$  continuously increases.

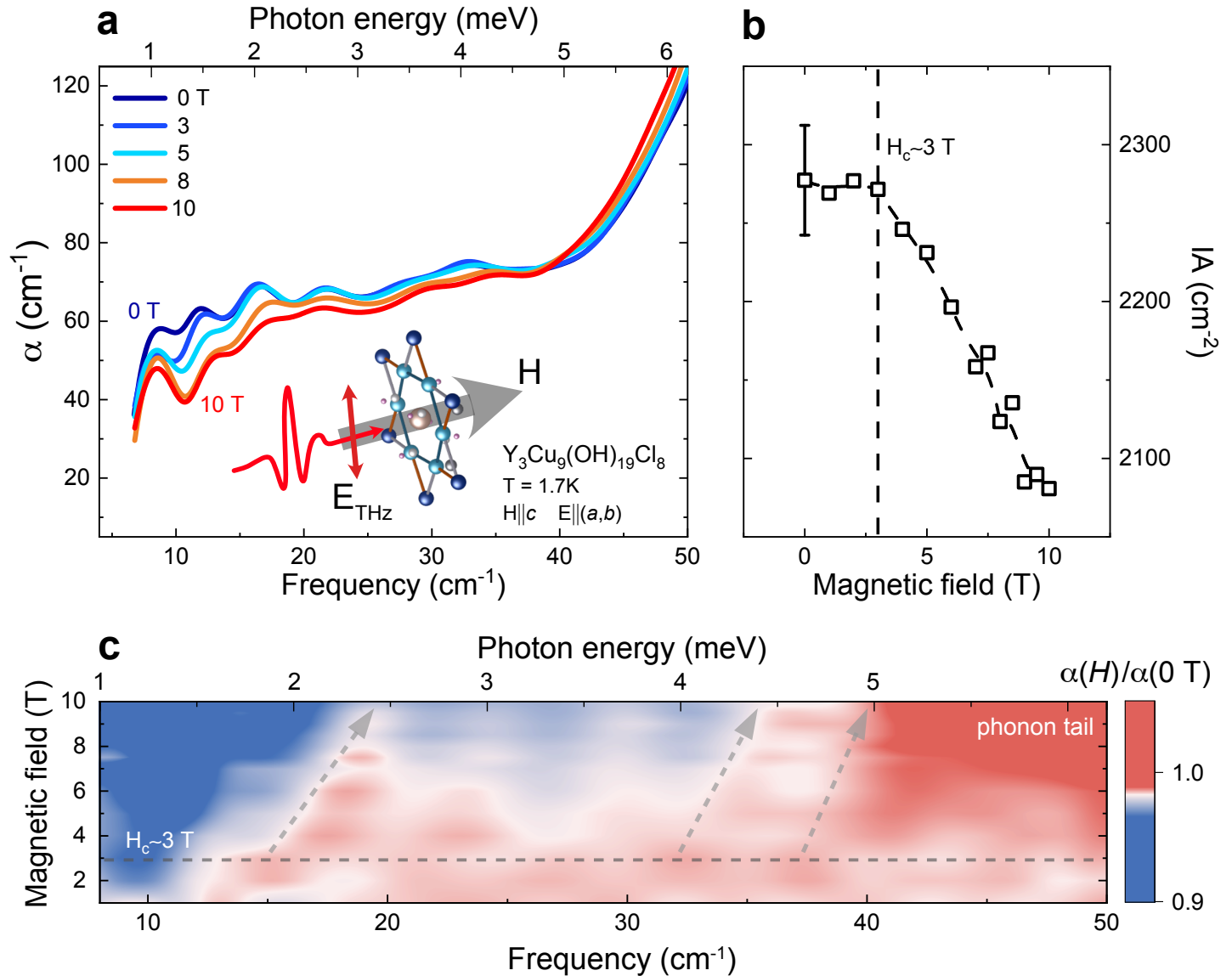


**Figure 4.** Result of magneto-THz spectroscopy at 1.7 K. a) Absorption coefficient  $\alpha$  under magnetic field in Faraday geometry, as depicted ( $\mathbf{H} \parallel c$ ,  $\mathbf{E}_{\text{THz}} \parallel (a,b)$ ). The THz continuum-like absorption decreases with increasing magnetic fields, confirming its magnetic origin. b) Integrated absorption coefficient  $IA$  (up to  $40\text{ cm}^{-1}$ ), exposing a critical magnetic field of  $H_c \sim 3\text{ T}$ . c) Contour plot of the relative absorption coefficient under magnetic field  $\alpha(H)/\alpha(0\text{ T})$ , normalized to zero field. The grey arrows indicate the field evolution of the onset of the continuum-like absorption and of the two peak-like features at  $32$  and  $37\text{ cm}^{-1}$ .

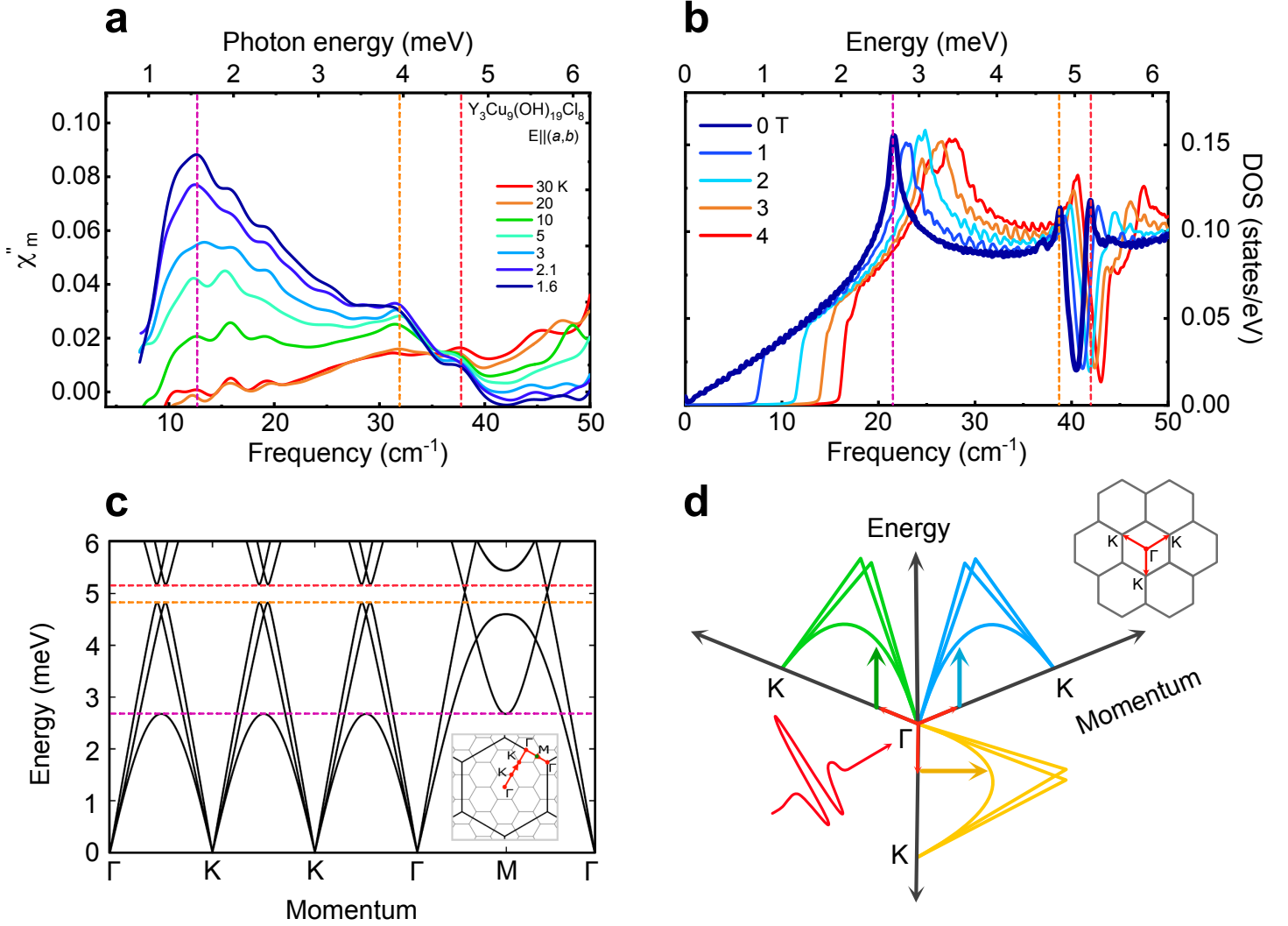


**Figure 5.** Three-center magnon excitations and theoretical spin-wave dispersion of Y-kapellasite. a) The frequency-dependent imaginary part of the magnetic susceptibility  $\chi''_m$  obtained from THz-TDS exposes the natural spectral form of the three-center magnon excitations. Three distinctive features are marked by vertical dashed lines. b) Spin density of states (SDOS) obtained from linear spin-wave theory calculations with and without magnetic field. The SDOS shows three characteristic energies below 6 meV with a high density of states (vertical dashed lines). c) Spin-wave dispersion of Y-kapellasite. Horizontal dashed lines: Corresponding to the energies in (b). Inset: Calculated path in the extended Brillouin zone (black hexagon). d) The three-center magnon process in momentum space, i.e. three spin excitations in the different magnetic sublattices (green, blue, and yellow color code) with  $0 \approx \sum_n \mathbf{q}_n$ .

# Supporting Information

## Multi-Center Magnon Excitations Open the Entire Brillouin Zone to Terahertz Magnetometry of Quantum Magnets

*Tobias Biesner, Seulki Roh, Aleksandar Razpopov, Jannis Willwater, Stefan Söllow, Ying Li, Katharina M. Zoch, Marisa Medarde, Jürgen Nuss, Denis Gorbunov, Yurii Skourski, Andrej Pustogow, Stuart E. Brown, Cornelius Krellner, Roser Valentí, Pascal Puphal, Martin Dressel*

### Contents

<b>1</b>	<b>Crystal growth</b>	<b>2</b>
<b>2</b>	<b>X-ray diffraction</b>	<b>3</b>
<b>3</b>	<b>ESR measurements</b>	<b>4</b>
<b>4</b>	<b>High-field magnetization</b>	<b>5</b>
<b>5</b>	<b>AC magnetization</b>	<b>7</b>
<b>6</b>	<b>Far-infrared phonons</b>	<b>8</b>
<b>7</b>	<b>Details of the phonon calculations</b>	<b>9</b>
<b>8</b>	<b>Extended data of THz-TDS</b>	<b>9</b>
<b>9</b>	<b>Determination of <math>\chi_m''</math></b>	<b>10</b>
<b>10</b>	<b>THz frequency-domain measurements</b>	<b>12</b>
<b>11</b>	<b>Magneto-optical THz-TDS</b>	<b>13</b>
<b>12</b>	<b>Details of the linear spin-wave theory calculations</b>	<b>14</b>
<b>13</b>	<b>Linear spin-wave theory calculations over an extended energy range</b>	<b>15</b>
<b>14</b>	<b>Calculation of <math>\chi_m''</math></b>	<b>16</b>
<b>15</b>	<b>Linear spin-wave theory calculations under magnetic field</b>	<b>17</b>
<b>16</b>	<b>Two-center magnon and three-center magnon excitation</b>	<b>19</b>
<b>17</b>	<b>Comparison with Herbertsmithite</b>	<b>20</b>

# 1 Crystal growth

The crystal growth of  $\text{Y}_3\text{Cu}_9(\text{OH})_{19}\text{Cl}_8$  was originally reported in Reference, <sup>[1]</sup> where 0.59 g  $\text{Y}_2\text{O}_3$ , 0.82 g  $\text{CuO}$ , and 0.89 g  $\text{CuCl}_2 \cdot 2(\text{H}_2\text{O})$  in 10 ml  $\text{H}_2\text{O}$  were heated up to the dissolution point of  $\text{Y}_2\text{O}_3$ , followed by a slow cooling to crystallize as sketched in **Figure S1a**. However, these crystals of an average size of  $1 \times 1 \times 1 \text{ mm}^3$  suffered from small  $\text{CuO}$  inclusions since the growth takes place on the surface of the polycrystalline  $\text{CuO}$  starting material, as the dissolution point of  $\text{Y}_2\text{O}_3$  and the crystallization point of the compound lie above the maximum in solubility of  $\text{CuO}$ . We thus optimized the synthesis via a horizontal external gradient growth method in a thick-walled quartz ampule by slowly dissolving  $\text{CuO}$  in a  $\text{YCl}_3\text{-H}_2\text{O}$  solution and transporting it to the cold end as depicted in Figure S1b. Here, the inclusion free hexagonal single crystals have an average size of  $3 \times 3 \times 1 \text{ mm}^3$  up to  $3 \times 3 \times 3 \text{ mm}^3$ , if grown over several weeks. The pictures of a single crystalline Y-kapellasite are displayed in Figure S1c and d, which show in the given thickness a transparent specimen without any visible impurity inclusions, but some terrace nucleation is apparent.

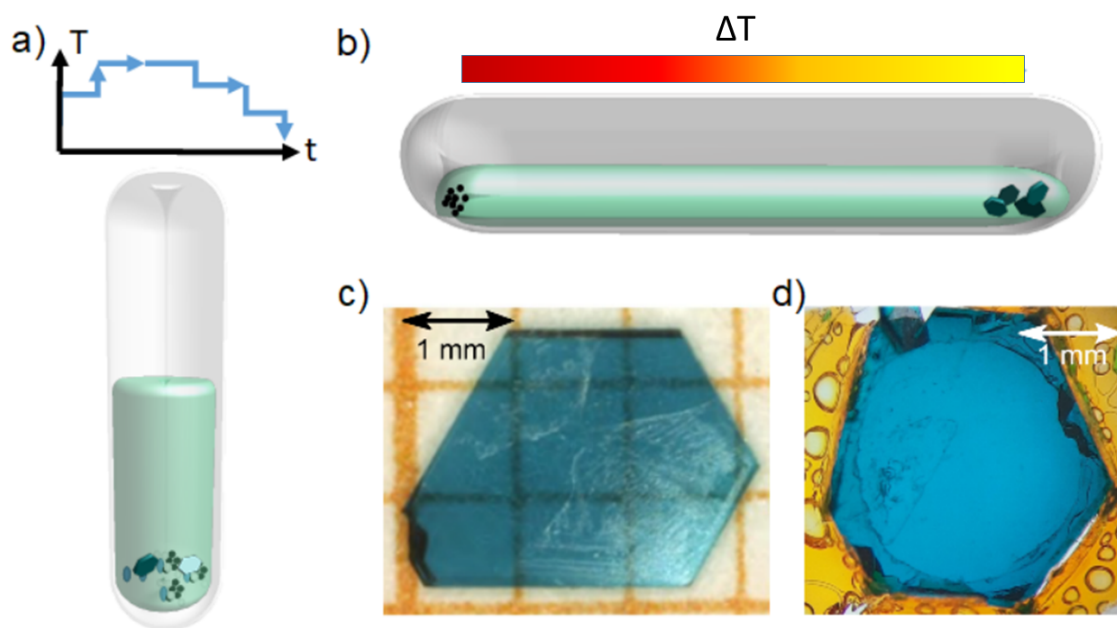


**Figure S1.** Improvement of the growing method of Y-kapellasite. a) Sketch of a thin-walled ampule that is heated and subsequently cooled in an autoclave. b) Sketch of the lying thick-walled quartz ampule that is exposed to an external gradient. Obtained Y-kapellasite single crystals: c) A single crystalline sample of Y-kapellasite with  $3 \times 3 \times 1 \text{ mm}^3$  size. d) A sample used in THz-TDS measurements, fixed on the sample holder.



## 2 X-ray diffraction

The structure of  $\text{Y}_3\text{Cu}_9(\text{OH})_{19}\text{Cl}_8$  was reported in Reference,<sup>[1]</sup> while for deuterated powder samples a different result was found in Reference<sup>[2]</sup> where, in contrast to the single crystal structure, the O1 site has no deuterium leading to the stoichiometry of  $\text{Y}_3\text{Cu}_9(\text{OD})_{18}\text{OCl}_8$ .

A recent report describes a synthesis of inclusion free crystals using  $\text{LiOH}$ ,  $\text{Y}(\text{NO}_3)_3 \cdot 6\text{H}_2\text{O}$  and  $\text{CuCl}_2 \cdot 2\text{H}_2\text{O}$  with another slightly varied structure, where a partial occupation of Y in the kagome plane is present.<sup>[3]</sup> This likely presents an example of a phase mixture with  $\text{YCu}_3(\text{OH})_6\text{Cl}_3$ .<sup>[4]</sup> This phase mixture leads to a magnetic transition around 11 K. We note that already the structure solution of  $\text{YCu}_3(\text{OH})_6\text{Cl}_3$  shows a phase mixture as partial occupation of Y out of the kagome plane is observed, which represents structure parts of  $\text{Y}_3\text{Cu}_9(\text{OH})_{19}\text{Cl}_8$ . For the large inclusion free single crystals, described in our paper, we performed single crystal diffraction to shed light on this various forms of structure. A crystal was broken under high viscosity oil and a  $150 \mu\text{m}$  piece was mounted with grease on a loop made of Kapton foil (Micromounts, MiTeGen, Ithaca, NY). Diffraction data were collected with a SMART APEX II CCD X-ray diffractometer (Bruker AXS, Karlsruhe, Germany) using graphite-monochromated  $\text{Mo-K}_\alpha$  radiation ( $\lambda = 0.71073 \text{ \AA}$ ) at low temperature  $T = 100(2) \text{ K}$ . **Figure S2** shows the XRD maps of the  $(hk0)$ ,  $(h0l)$ , and  $(0kl)$  reciprocal lattice planes of the  $\text{Y}_3\text{Cu}_9(\text{OH})_{19}\text{Cl}_8$  single crystal. We can confirm the published  $\text{Y}_3\text{Cu}_9(\text{OH})_{19}\text{Cl}_8$  structure<sup>[1]</sup> with a goodness of the fit of 1.1 and find no disorder on the Y site. Note that the crystal under investigation showed reticular-merohedral twinning (reverse-obverse twin). This was taken into account during structure refinement, the twin volume fractions were determined as 0.847(2) and 0.153(2), respectively.

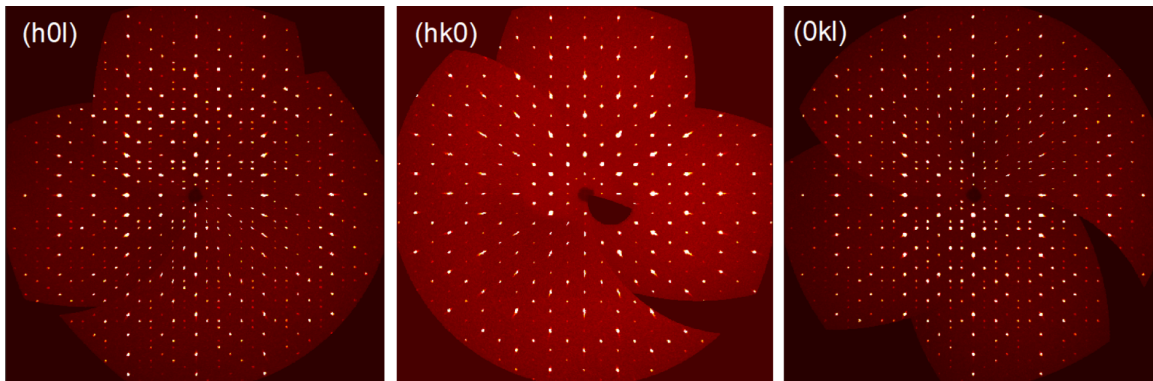


**Figure S2.** Single crystal diffraction. XRD maps of the  $(h0l)$ ,  $(hk0)$ , and  $(0kl)$  planes of the investigated  $\text{Y}_3\text{Cu}_9(\text{OH})_{19}\text{Cl}_8$  crystal.

### 3 ESR measurements

Temperature-dependent electron spin resonance (ESR) measurements in the X-band frequency ( $f = 9.8$  GHz) were carried out employing a Bruker (EMXplus) cw-spectrometer and an Oxford Instruments He-flow cryostat. The results are shown in **Figure S3**. The external magnetic field is applied within the kagome planes  $\mathbf{H} \parallel (a, b)$  and the microwave field  $\mathbf{h}$  is oriented along the  $c$ -axis. In Figure S3a, a broad contribution evolves in the derivative of the absorbed microwave power  $dP/dH$  below the onset of short-range magnetic correlations,  $T \approx 30$  K. Further cooling results in a strong increase of the overall amplitude and a shift of the contribution to lower magnetic fields. This broad feature agrees well with the derivative of a Lorentzian (red dashed line). Additional small resonances develop upon cooling, possibly related to tiny magnetic impurities in the sample. The good agreement between the temperature scales of the NMR measurements (see main text) and the ESR investigation suggests short-range magnetic correlations to be the main source of this resonance.

In general, the absorbed microwave power is proportional to the imaginary part of the magnetic susceptibility,  $P \propto \chi''$ . Hence,  $\chi''$  is obtained by integrating the measured derivative of the absorbed power  $dP/dH$  over the magnetic field  $H$  (inset of Figure S3a). The electron spin susceptibility  $\chi_s^e$  (Figure S3b, as shown in **Figure 2** of the main text) is directly proportional to the intensity of the ESR absorption line by the Kramers-Kronig sum rule:  $\chi_s^e \propto \int_0^\infty P(H)dH = I^{[5]}$  and therefore obtained from the intensity of the Lorentz fits of  $dP/dH$ .

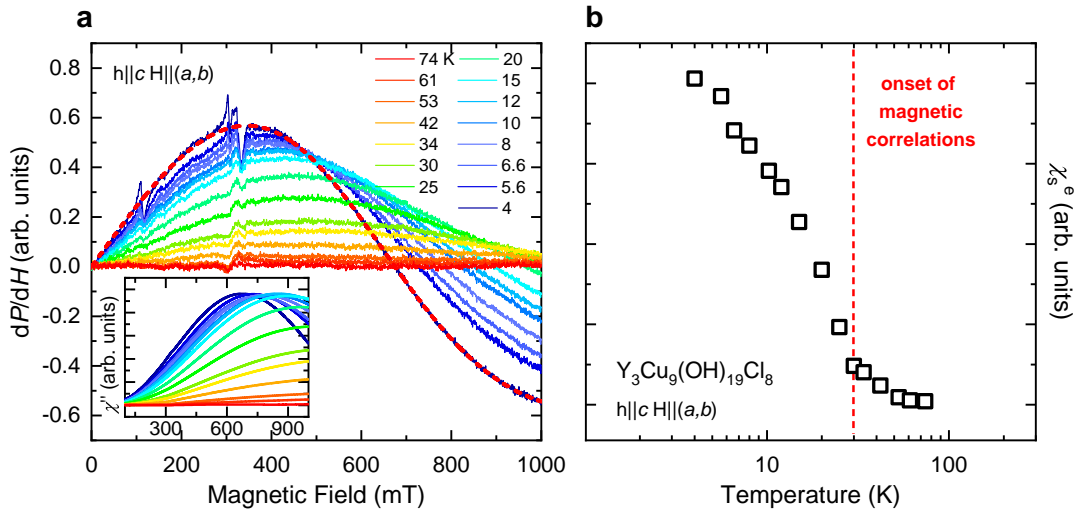


**Figure S3.** X-band ESR measurements of Y-kapellasite. a) Derivative of the absorbed microwave power with respect to the magnetic field: External magnetic field  $\mathbf{H} \parallel (a, b)$  with microwave field ( $f = 9.8$  GHz)  $\mathbf{h} \parallel c$ . Upon cooling below the onset of short-range magnetic correlations, a large Lorentzian feature starts to develop. Red dashed line: Fit of the Lorentzian derivative for  $T = 4$  K, for example. Inset of (a):  $\chi''$  obtained by the integration of  $dP/dH$ . b) Electron spin susceptibility  $\chi_s^e$ , obtained from the Lorentzian analysis of  $dP/dH$ . A strong increase can be seen at the onset of short-range magnetic correlations (vertical red dashed line).

## 4 High-field magnetization

In order to investigate the low-temperature magnetic transitions further, we performed high-field magnetization measurements. For the measurements with a field parallel to the kagome plane, a single crystal with a total mass of 7.2 mg was aligned in a Laue diffractometer to confirm high crystalline quality. In order to assemble enough material for the configuration with the magnetic field perpendicular to the kagome plane (parallel to the  $c$ -axis), an array of seven small single crystals with a total weight of 6.8 mg was prepared. The magnetization was measured as a function of temperature and of field up to 5 T with a commercial SQUID-magnetometer. Subsequently, the magnetization was measured at the high field laboratory in Dresden (HLD-EMFL) at temperatures between 0.5 K and 30 K with fields up to 55 T. A coaxial pick-up coil system<sup>[6]</sup> was used to measure the relative magnetization. Absolute values were scaled by using the data from the SQUID measurements.

The high-field magnetization measurements are presented in **Figure S4**. Above  $T = 5$  K the response shows a close-to-linear dependence on the external magnetic field with subtle features developing as the temperature approaches  $T_N \approx 2.2$  K. Below  $T_N$ , a clear magnetization plateau is formed slightly above 15 T, which can be seen in both in-plane and out-of-plane measurements, with plateau values of  $0.21 \mu_B$  for the  $a, b$ -plane and  $0.18 \mu_B$  for the  $c$ -axis at  $T = 1.5$  K, Figure S4a and c. Increasing the field further, the magnetization rises again by deviating from the plateau response. The differential magnetization (Figure S4b and d) reveals a small change of the slope between 40 to 45 T, suggesting another magnetization plateau with  $0.37 \mu_B$  for the  $a, b$ -plane and  $0.33 \mu_B$  for the  $c$ -axis. While the lower field plateaus are robust even in the  $^3\text{He}$  measurements, probing down to  $T = 0.49$  K, the more subtle slope changes at high fields are hard to observe here. Considering the similar magnetization for in-plane and out-of-plane orientations, our measurements show that the magnetic anisotropy is rather weak for Y-kapellasite.

The emergence of two plateau-like features at low temperatures around  $1/6$  and  $1/3$  of full magnetization suggests an involvement of the spins in the hexagon of the kagome lattice in intermediate magnetic phases before the saturation. Similar observations were made, for instance, in the distorted kagome magnet Volborthite.<sup>[7,8]</sup>

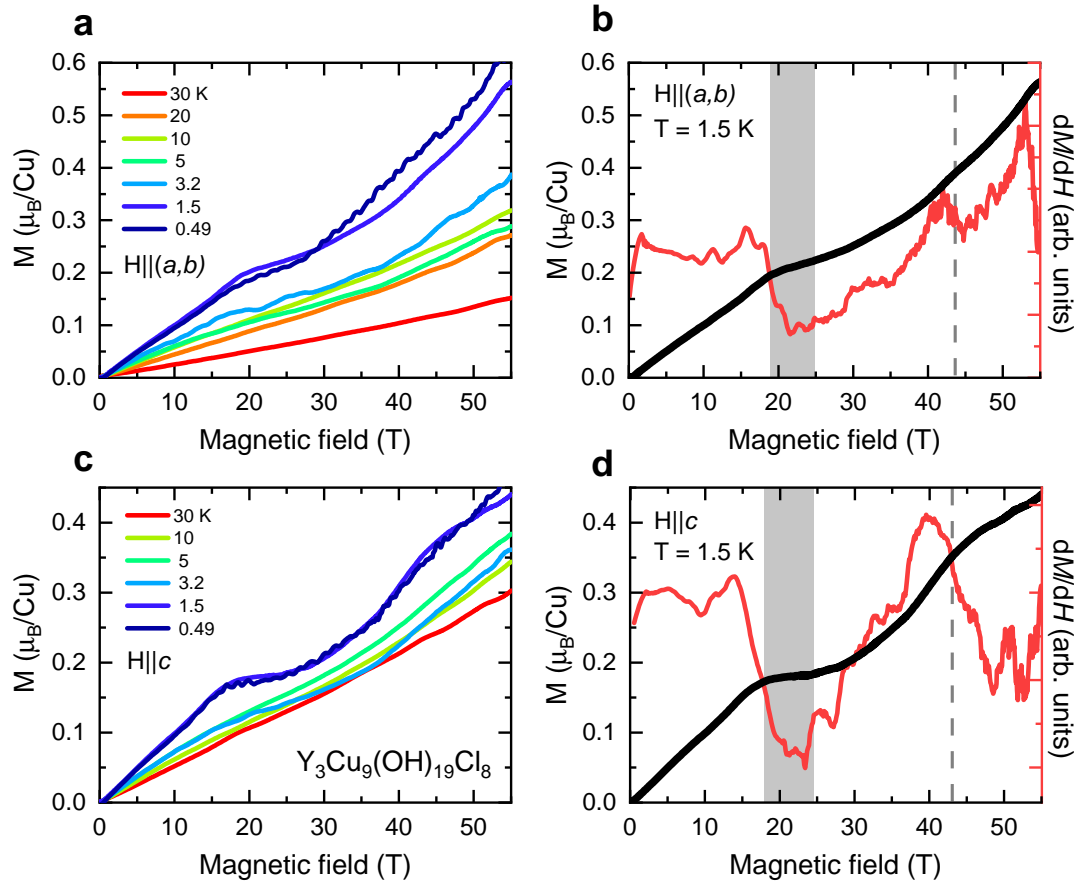


**Figure S4.** Magnetization of Y-kapellasite in pulsed magnetic fields up to **55 T**. a) Magnetization  $M$  in the  $a, b$ -plane,  $\mathbf{H} \parallel (a, b)$ . b) Magnetization  $M$  (black line, left axis) in comparison to differential magnetization  $dM/dH$  (red line, right axis) at  $T = 1.5$  K. c,d) Results for the  $c$ -axis,  $\mathbf{H} \parallel c$ .

## 5 AC magnetization

Dc magnetic susceptibility, shown in the main manuscript, and ac magnetic susceptibility measurements were carried out on these crystals in a range of 0.5–10 K, 0–6 T, and 99–1024 Hz, using a Quantum Design Magnetic Property Measurements System (MPMS) equipped with a  $^3\text{He}$  insert and a Physical Properties Measurement System (PPMS) utilizing the standard ACMS option in the range of 2–300 K, 0–6 T, and 99–9999 Hz. Results are shown in **Figure S5**. With increasing the frequency of the in-plane ac magnetic field of 0.38 mT the imaginary part of the magnetization  $M''$  starts to rise, Figure S5a. Reaching a frequency of around 10 kHz,  $M''$  shows a broad contribution between 30 K and 100 K, centered at  $T = 50$  K, independent of the cooling protocol. Around  $T = 2$  K, Figure S5b, a small kink becomes visible for increased frequencies (333–1024 Hz), possibly related to the onset of magnetic ordering. Further cooling results in a strong frequency-dependent behavior. While frequencies below  $f = 800$  Hz lead to comparable temperature dependencies, at  $f = 1024$  Hz,  $M''$  increases below 0.8 K. The enhancement of  $M''$  at low temperatures and the broad contribution above  $T = 30$  K imply the occurrence of an absorption mechanism for oscillating fields, connected to the long-range magnetic order and the onset of short-range magnetic correlations.

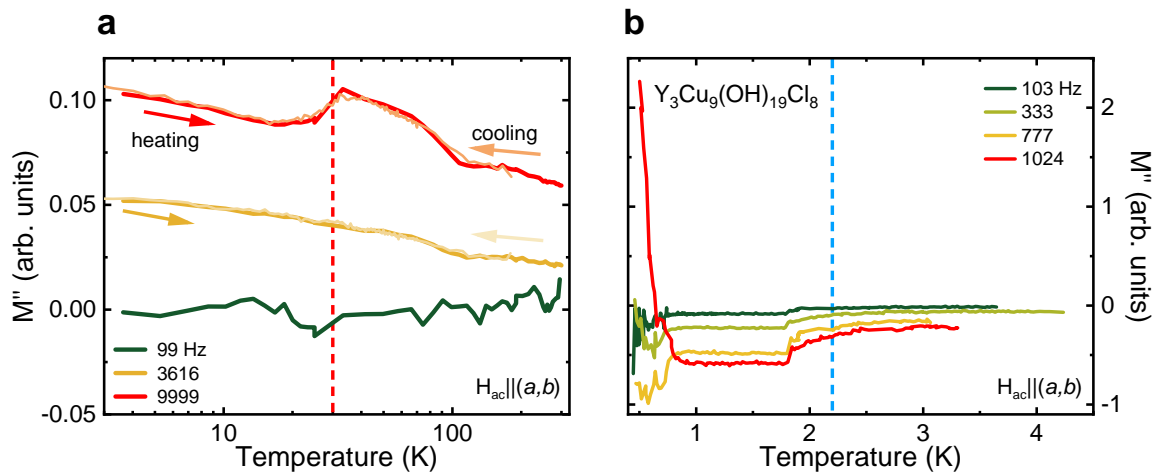


**Figure S5.** AC magnetization of Y-kapellasite. Imaginary part of the magnetization  $M''$  with an in-plane oscillating field ( $H_{ac} \parallel (a, b)$ ) of 0.38 mT for various oscillation frequencies. a) With increasing the frequency,  $M''$  starts to rise. The broad contribution between 100 K and 30 K might be related to the onset of short-range magnetic correlations (red dashed line),  $T \approx 30$  K. b) At low temperatures,  $M''$  starts to increase for  $f = 1024$  Hz below  $T_N = 2.2$  K (blue dashed line).

## 6 Far-infrared phonons

In order to separate the phonon modes from the observed THz response, we performed infrared spectroscopy in an extended frequency range. Far-infrared measurements were carried out in reflection geometry on thick crystals (over 2 mm thickness), using a Bruker 113v FTIR spectrometer equipped with an *in-situ* gold evaporation technique.<sup>[9]</sup> With the Kramers-Kronig analysis, optical properties are calculated.<sup>[10,11]</sup> Results in the spectral area of interest are shown in **Figure S6**. Several vibrational modes were observed in both, in-plane and out-of-plane, measurements. With cooling down to  $T = 3$  K, most of the phonons show a sharpening and a blueshift, as generally expected. Interesting behavior is observed for the in-plane  $80\text{ cm}^{-1}$  feature which exhibits a redshift with cooling, manifesting the negative Grüneisen parameter, i.e. a lattice instability. A magnetoelastic coupling scenario might be possible, similar to the case of Herbertsmithite.<sup>[12]</sup> A coupling of the phonons and the magnetic texture of Y-kapellasite is indeed corroborated by our magneto-THz results (main text), revealing a shift of the phonon tail of the lowest  $E_u$  mode under magnetic field.

Phonon calculations were performed and put in relation to the experimental results. Comparing the observed phonon modes to our calculations, a good agreement of the resonance frequencies is visible, cf. Figure S6a and c. From the density functional theory (DFT) calculations, the two lowest frequency phonon modes are expected to be at  $44.9\text{ cm}^{-1}$  ( $E_u$ ) and  $47.8\text{ cm}^{-1}$  ( $A_u$ ). In the infrared spectra, these two modes are not well pronounced. However, the phonon tails observed in the THz spectra above  $40\text{ cm}^{-1}$  (main text) match well with these frequencies, confirming the influence of phonons at high frequency but not at low frequencies in our THz range.

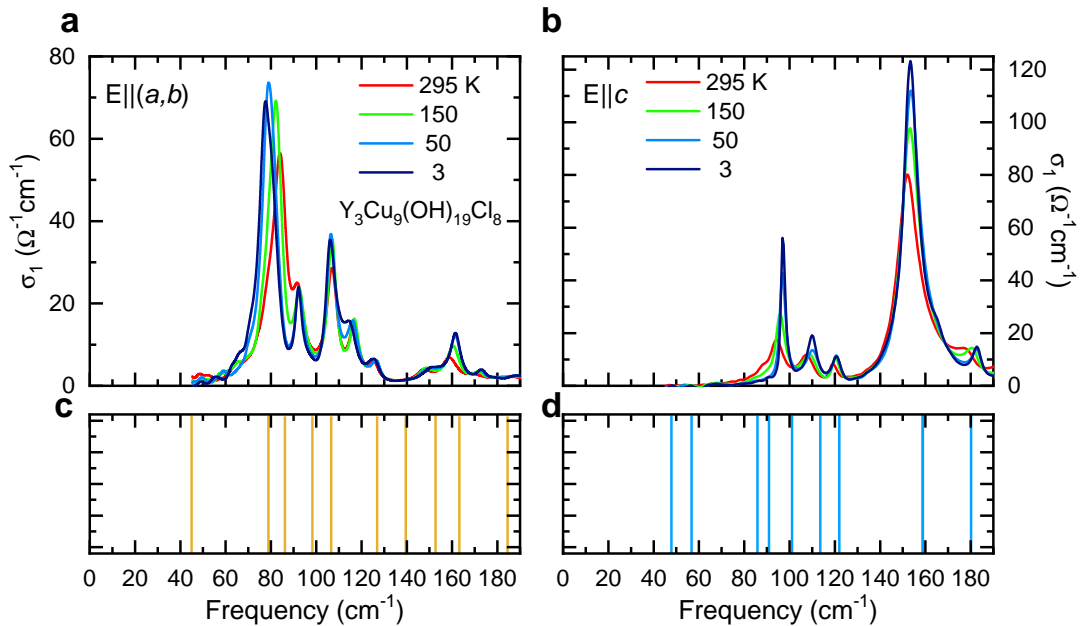


**Figure S6.** Infrared spectra and expected phonon frequencies (DFT calculation). The far-infrared optical conductivity  $\sigma_1$  is dominated by multiple phononic contributions: a) in-plane measurements  $\mathbf{E} \parallel (a, b)$  and b) out-of-plane  $\mathbf{E} \parallel c$  response. c,d) Calculated  $E_u$  and  $A_u$  phonon mode frequencies, respectively.

## 7 Details of the phonon calculations

*Ab initio* vibrational studies were performed using the crystal structure of  $\text{Y}_3\text{Cu}_9(\text{OH})_{19}\text{Cl}_8$  relaxed from the experimental one at 173 K.<sup>[1]</sup> In order to keep the symmetry and describe the fractional occupancy of H reported in Reference,<sup>[1]</sup> we used the virtual crystal approximation (VCA), where we considered fictitious 'virtual' atoms that interpolate between the behavior of the H atom and a vacancy. The validity of such an approximation for simulating possible vacancy effects has been tested in the past.<sup>[13,14]</sup> The phonon frequencies were calculated by diagonalizing the dynamical matrices using the PHONOPY package.<sup>[15,16]</sup> The dynamical matrices were constructed from the force constants determined from the finite displacements in the conventional unit cell,<sup>[17]</sup> which is equivalent to three unit cells in Herbertsmithite.<sup>[12]</sup> The density functional calculations were performed within the Perdew-Burke-Ernzerhof parametrization of the generalized gradient approximation<sup>[18]</sup> implemented in the Vienna package (VASP).<sup>[19,20,21]</sup> The Brillouin zone was sampled with a  $4 \times 4 \times 4$  k-point mesh, and the plane-wave cutoff was set at 520 eV.

## 8 Extended data of THz-TDS

Temperature-dependent THz-TDS measurements are carried out in transmission geometry employing a Teraview Terapulse 4000 THz-TDS spectrometer along with a He-bath cryostat on oriented single crystals. The time-domain electric fields, which are directly measured from our THz spectrometer, are displayed in **Figure S7a** for in-plane. By performing the Fast Fourier Transformation (FFT), the frequency-dependent power spectrum  $\tilde{E}_{sample}(\omega)$  was obtained. Then, the complex transmission  $\tilde{T}r(\omega)$  was calculated by referencing to the empty hole of sample holder,  $\tilde{E}_{ref}(\omega)$ :  $\tilde{T}r(\omega) = \tilde{E}_{sample}(\omega)/\tilde{E}_{ref}(\omega)$ . The absorption coefficient of the sample is related to the transmittance  $Tr(\omega)$  (real part of  $\tilde{T}r$ ) via the Beer-Lambert law:  $\alpha(\omega) = -\ln\{Tr(\omega)\}/d$ , where  $d$  is the thickness of the sample. The absorption coefficient spectra for all measured temperatures are shown in Figure S7b.

The integrated absorption coefficient, which is used to analyze the spectra in the main text,  $IA = \int \alpha(\omega) d\omega$  is proportional to the optical spectral weight  $SW = \int \sigma(\omega) d\omega$  with the relation  $\alpha(\omega) = 4\pi\sigma(\omega)/n(\omega)$ , where  $\sigma$  is optical conductivity and  $n$  is index of refraction.<sup>[10,11]</sup>

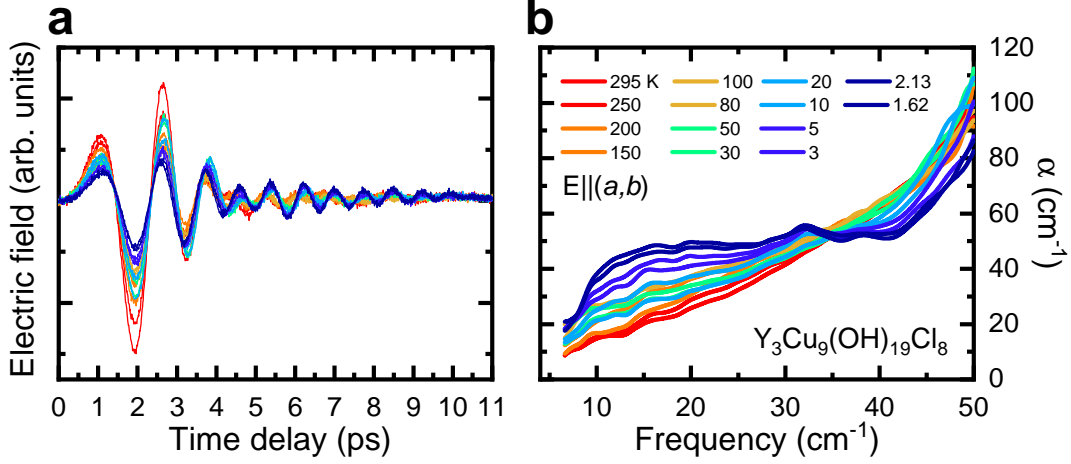


**Figure S7.** THz-TDS result for all measured temperatures. a,b) Time-domain electric field and absorption coefficient for the in-plane  $\mathbf{E} \parallel (a, b)$  response, respectively.

## 9 Determination of $\chi_m''$

In the main text we show  $\chi_m'' = \text{Im}\{\tilde{\chi}_m(\omega)\}$ , where  $\tilde{\chi}_m(\omega) \approx \frac{2ic}{\sqrt{\tilde{\epsilon}_{ref}}\omega d} \ln\left\{\frac{\tilde{T}r_{ref}}{\tilde{T}r}\right\}$ . Here, the low-temperature magnetic susceptibility  $\tilde{\chi}_m$  is extracted from THz-TDS measurements by referencing to the spectra at temperatures above the magnetic ordering (or onset of magnetic interaction). Such an approach was used in References [22, 23, 24, 25, 26, 27] and proven to be robust in the class of insulating quantum magnets since the electronic contributions are located at much higher frequencies. In the following,  $\tilde{\chi}_m(\omega)$  is derived using this approach, a more detailed explanation can be found in Reference. [25] In general, complex transmission through the sample with thickness  $d$ , can be written as  $\tilde{T}r(\omega) = 4 \frac{Z_0 \tilde{Z}_s}{(Z_0 + \tilde{Z}_s)^2} \exp\left\{i \frac{\omega d}{c} (\tilde{n} - 1)\right\}$ , where  $Z_0 = 377 \Omega$  and  $\tilde{Z}_s = \sqrt{\frac{\tilde{\mu}}{\tilde{\epsilon}}}$  is the complex impedance of the sample with permittivity  $\tilde{\epsilon}$  and magnetic permeability  $\tilde{\mu}$ .  $\tilde{n} = \sqrt{\tilde{\epsilon}\tilde{\mu}}$  is the index of refraction of the sample. [11, 28] Rewriting the complex transmission in terms of  $\tilde{\epsilon}$  and  $\tilde{\mu}$  leads to

$$\tilde{T}r(\omega) = \frac{4\sqrt{\tilde{\epsilon}\tilde{\mu}}}{(\sqrt{\tilde{\epsilon}} + \sqrt{\tilde{\mu}})^2} \exp\left\{i \frac{\omega d}{c} (\sqrt{\tilde{\epsilon}\tilde{\mu}} - 1)\right\}. \quad (1)$$

For the magnetic permeability we can write  $\tilde{\mu} = 1 + \tilde{\chi}_m$ . By assuming  $\tilde{\chi}_m \ll 1$  and  $\sqrt{\tilde{\mu}} \approx 1 + \tilde{\chi}_m/2$  it reads:

$$\tilde{T}r(\omega) \approx \frac{4\sqrt{\tilde{\epsilon}}(1 + \tilde{\chi}_m/2)}{(\sqrt{\tilde{\epsilon}} + 1 + \tilde{\chi}_m/2)^2} \exp\left\{i \frac{\omega d}{c} (\sqrt{\tilde{\epsilon}}(1 + \tilde{\chi}_m/2) - 1)\right\}. \quad (2)$$

It can furthermore be simplified as:

$$\tilde{T}r(\omega) \approx \exp\left\{i \frac{\omega d}{c} (\sqrt{\tilde{\epsilon}}(1 + \tilde{\chi}_m/2) - 1)\right\}, \quad (3)$$

since the exponential term is dominating in Equation 2. To extract  $\tilde{\chi}_m$  from Equation 3, the dielectric contribution needs to be subtracted.  $\tilde{T}r$  can be referenced to a temperature, where  $\tilde{\mu} \approx 1$ , i.e. above the onset of magnetic interactions. Here, the complex transmission reads  $\tilde{T}r_{ref} \approx \exp\left\{i \frac{\omega d}{c} (\sqrt{\tilde{\epsilon}_{ref}} - 1)\right\}$ . Under the assumption that the dielectric properties (phononic or electronic contributions) in the THz range do not change considerably below the reference temperature we can write:  $\tilde{\epsilon}_{ref} \approx \tilde{\epsilon}$  and therefore



---

$\frac{\tilde{T}r}{T_{ref}} \approx \exp \left\{ i \frac{\sqrt{\tilde{\epsilon}_{ref}} \omega d}{2c} \tilde{\chi}_m \right\}$ . Inverting this leads to:

$$\tilde{\chi}_m(\omega) \approx \frac{2ic}{\sqrt{\tilde{\epsilon}_{ref}} \omega d} \ln \left\{ \frac{\tilde{T}r_{ref}}{\tilde{T}r} \right\}. \quad (4)$$

## 10 THz frequency-domain measurements

THz frequency-domain spectroscopy (THz-FDS) was carried out using a frequency-tunable backward-wave-oscillator (BWO), generating continuous, coherent, and monochromatic THz radiation with a Go-lay cell serving as a detector and a He-bath cryostat for temperature control.<sup>[29]</sup> The transmittance was measured by recording the intensity of the THz radiation transmitted through the sample and referenced to the empty hole of the sample holder. Results are shown in **Figure S8**. In THz-FDS, a series of single frequency measurements were repeated to cover the frequency range between 7.5 to 13  $\text{cm}^{-1}$  which lacks the time resolution compared to the THz-TDS. Multiple reflections of the incident light between the parallel surfaces of transparent sample generate the pronounced Fabry-Perot oscillation pattern in Figure S8. In the THz-TDS, this effect can be avoided by controlling the time window. Nevertheless, the THz-FDS measurements are in good qualitative agreement with the THz-TDS results. Upon cooling to  $T = 100$  K, the transmittance gets suppressed supporting the increase in the integrated absorption coefficient  $IA$  for the in-plane orientation as presented in the main text (c.f. inset of Figure S8). From  $T = 100$  K to  $T = 20$  K, the transmittance rises again corresponding to a drop of the  $IA$ . Further cooling down to  $T = 1.65$  K, a strong suppression of the transmittance is observed, in accordance with a rise of the  $IA$  due to the excitations of the three-center magnon.

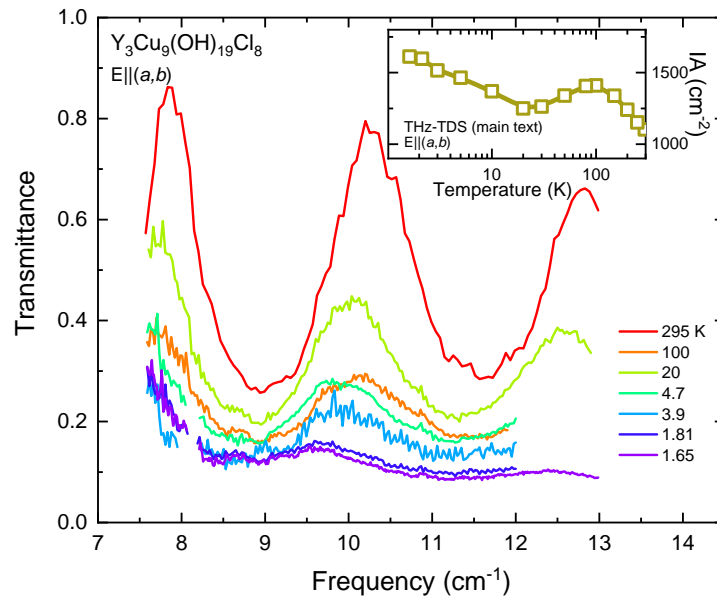


**Figure S8.** THz-FDS measurements. The temperature-dependent evolution of the transmittance is in good agreement with the  $IA$  obtained by THz-TDS (inset). The oscillation pattern in THz-FDS measurements originates from multiple internal reflections, as the transparent sample serves as a Fabry-Perot resonator, an etalon.

## 11 Magneto-optical THz-TDS

For magneto-optical THz-TDS measurements, a superconducting magnet (Oxford Instruments) is used to apply a static external magnetic field up to  $H = 10$  T in Faraday geometry ( $\mathbf{E}_{THz} \parallel (a, b)$ ,  $\mathbf{H} \parallel c$ ) with temperature down to  $T = 1.7$  K. **Figure S9** shows the time-domain electric fields and the corresponding absorption coefficient over the full magnetic field range. With increasing the magnetic field, the main pulse (below 4 ps) increases, while the extended-time oscillations lose intensity, c.f. Figure S9a. In the absorption coefficient, Figure S9b, this field dependency corresponds to a decrease of the continuum-like feature and the peak-like contributions between  $30 - 40$   $\text{cm}^{-1}$  as expected from the spin-wave theory. As well, the phonon-tail (above  $40$   $\text{cm}^{-1}$ ) slightly shifts to lower frequencies.

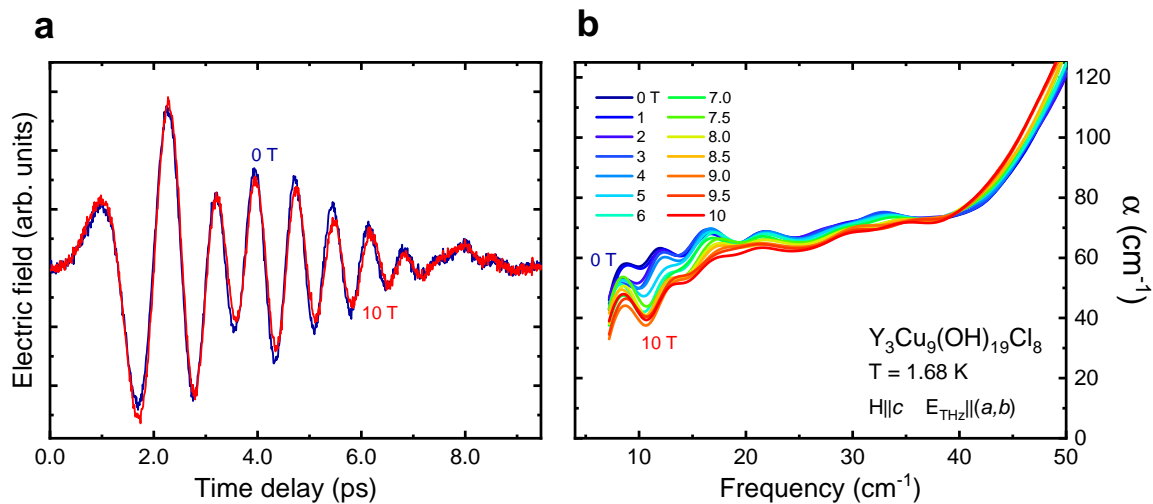


**Figure S9.** Magneto-optical THz-TDS result over the full magnetic field range. a,b) Time domain electric field and absorption coefficient in Faraday geometry ( $\mathbf{E}_{THz} \parallel (a, b)$ ,  $\mathbf{H} \parallel c$ ) at  $T = 1.68$  K, respectively.

## 12 Details of the linear spin-wave theory calculations

We performed linear spin-wave theory (LSWT) to calculate the magnon dispersion and magnon density of states (shown in **Figure S10**) as implemented in SpinW 3.0.<sup>[30]</sup> The effective Hamiltonian for Y-kapellasite is given by a spin-1/2 Heisenberg Hamiltonian

$$H = \sum_{\langle i,j \rangle} J_{i,j} \mathbf{S}_i \mathbf{S}_j, \quad (5)$$

where the sum goes over the first nearest neighbors (NN). The distortions in the lattice lead to three different NN couplings  $J = 154.4$  K,  $J_{\diamond} = 134.2$  K, and  $J' = 8.7$  K which have been calculated via DFT+U and the total energy mapping analysis.<sup>[31]</sup> The classical ground state was optimized by non-restricted energy optimization. The obtained classical ground state is given by a coplanar state with an ordering vector  $\mathbf{Q} = (1/3, 1/3)$ . The magnon energy dispersion is calculated on 1000 k-points along the path  $\Gamma$ -K-M- $\Gamma$  as shown in the inset of the right panel in Figure S10. The magnon density of states is calculated on a  $100 \times 100 \times 100$  k-mesh by the definition

$$DOS(E) = \frac{1}{N} \sum_i^N \delta(E - E_i), \quad (6)$$

where  $E$  is the energy and  $E_i$  is the magnon energy with momentum  $\mathbf{q}$ . The Dirac delta function was approximated by a Lorentzian function

$$\delta_{\epsilon}(x) = \frac{1}{\pi} \frac{\epsilon}{x^2 + \epsilon^2}, \quad (7)$$

with  $\epsilon = 0.01$  and energy resolution 0.01 meV.

### 13 Linear spin-wave theory calculations over an extended energy range

Figure S10 shows the spin dispersion and spin density of states (DOS) over an extended energy range obtained from linear spin-wave theory (LSWT). Besides the three-peak structure mentioned in the main text, there are several high-energy peaks in the DOS. For the comparison between the  $\mathbf{q} = 0$  excitation and multi-center magnon excitation ( $\Delta\mathbf{q} = 0$ ), we display the corresponding DOS curves ( $\mathbf{q} = 0$  and over the entire Brillouin zone) in Figure S10 (left panel). The  $\mathbf{q} = 0$  DOS mainly consists of three excitations ( $E = 0$  meV Goldstone mode, around  $E = 7.4$  meV, and  $E = 8.4$  meV). Note that no excitations are expected in our experimental range (1 - 6 meV) within the  $\mathbf{q} = 0$  limit which calls for the multi-center magnon picture facilitating the  $\Delta\mathbf{q} = 0$  process. The latter two,  $\mathbf{q} = 0$  magnons,  $E = 7.4$  meV and  $E = 8.4$  meV, are located in the energy-range of the far-infrared phonon modes, which might be related to spin-phonon coupling as suggested in main text.

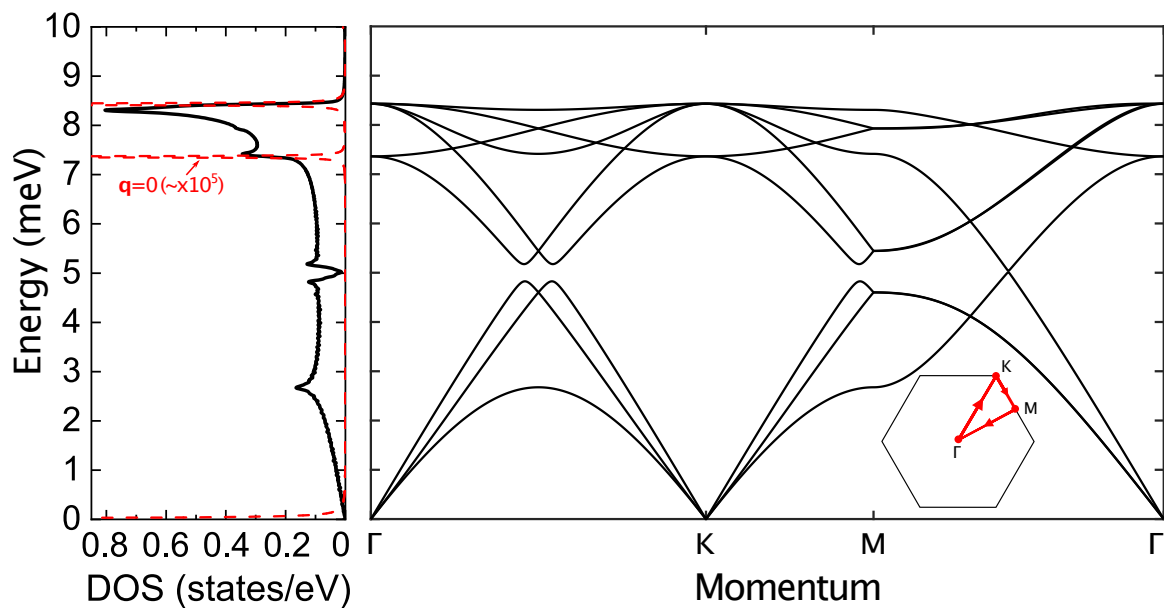


**Figure S10.** LSWT calculations. Left panel: DOS, black line: Integrated over the full Brillouin zone and red dashed line:  $\mathbf{q} = 0$  contribution (scaled by a factor of  $\sim 10^5$ ). Right panel: LSWT dispersion over an extended energy range. The inset shows the first Brillouin zone. The magnon dispersion has been calculated along the red arrows.

## 14 Calculation of $\chi_m''$

To confirm the spectral shape of the multi-center magnon and further compare directly between experiment and theory, we compute the imaginary part of the frequency-dependent magnetic susceptibility  $\chi_m'' = \text{Im}\{\tilde{\chi}_m(\omega)\}$  expected for the multi-center magnon absorption using the following relation<sup>[32]</sup>

$$\text{Im}\{\tilde{\chi}_m(\omega)\} = \gamma \sum_q \sum_{\alpha,\beta} h_\alpha h_\beta \text{Im}\{\chi_{\alpha,\beta}^{SS}(q, \omega)\}, \quad (8)$$

where  $\gamma$  is a constant,  $q$  is the momentum in the extended Brillouin zone, the summation  $\alpha$  and  $\beta$  goes over the Cartesian components,  $\chi_{\alpha,\beta}^{SS}(q, \omega)$  is the spin susceptibility, and  $h$  is the orientation of the THz magnetic field. At zero temperature the imaginary part of the spin susceptibility is related to the spin-spin correlation function  $S_{\alpha,\beta}$ :

$$\text{Im}\{\chi_{\alpha,\beta}^{SS}(q, \omega)\} = S_{\alpha,\beta}(q, \omega), \quad (9)$$

where the spin-spin correlation function is computed within the SpinW 3.0 frame work.<sup>[30]</sup> The energy resolution of  $\text{Im}\{\tilde{\chi}_m(\omega)\}$  is 0.1 meV with broadening of 0.1.

Results are shown in **Figure S11**. As discussed in the main text, the experimental and theoretical energy scales are slightly shifted with respect to each other (about 1 meV). In the calculation, a pronounced, asymmetric peak (at around 2.7 meV), corresponding to the first peak in SDOS (same energy) is well-reproduced. Comparing within the experimentally accessible range, the overall shape shows a nice agreement including the double peak/ dip-like structure (around 4 to 4.6 meV in experiment, 5 meV in calculation) validating the multi-magnon scenario once more. The calculation shows a low-energy contribution (below 2 meV). This feature is outside our experimental range, but perhaps the extra broadening of the experimental peak might already contain the effect of this contribution.

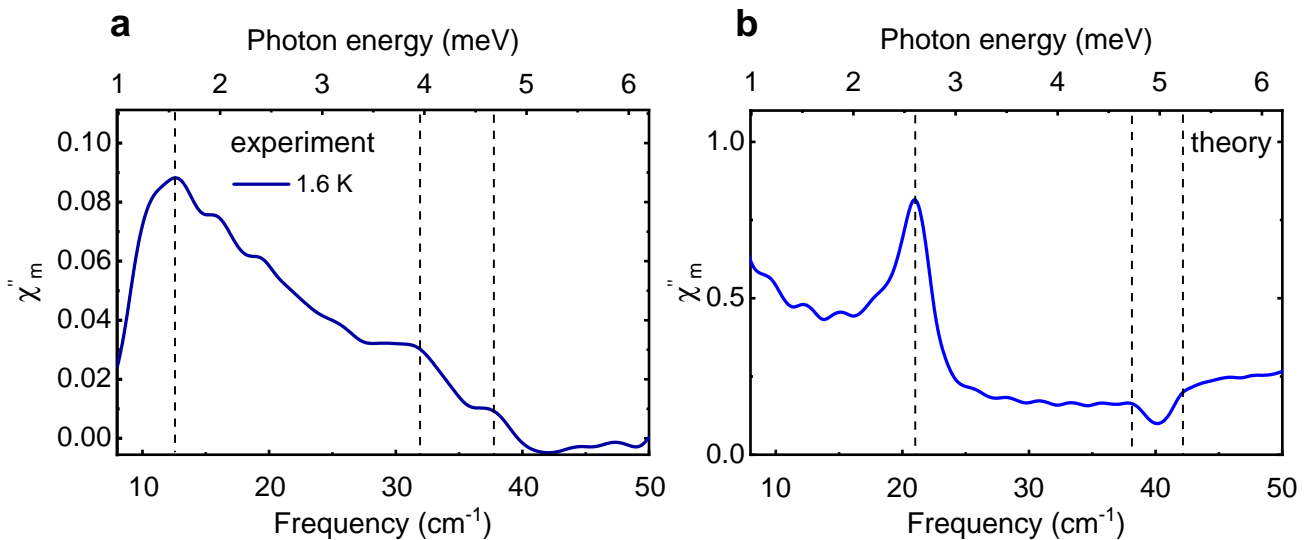


**Figure S11.** Comparison between (a) experimentally and (b) theoretically determined dynamic magnetic susceptibility  $\chi_m''$ . All experimental features are reproduced by the calculation. Note that the energy scale between experiment and theory is shifted by a small offset of about 1 meV.

## 15 Linear spin-wave theory calculations under magnetic field

**Figure S12** shows the calculated spin dispersion under external magnetic field. With increasing magnetic fields, the low-energy dispersion (0 to 3 meV) becomes gapped at the  $\Gamma$  and  $K$  points and shifts to higher energies, partially lifting the degeneracy of the three lowest magnon bands. As well, shifts of the characteristic energy scales (between 3 and 6 meV, colored dashed lines), discussed in the main text, to higher energies are observable.

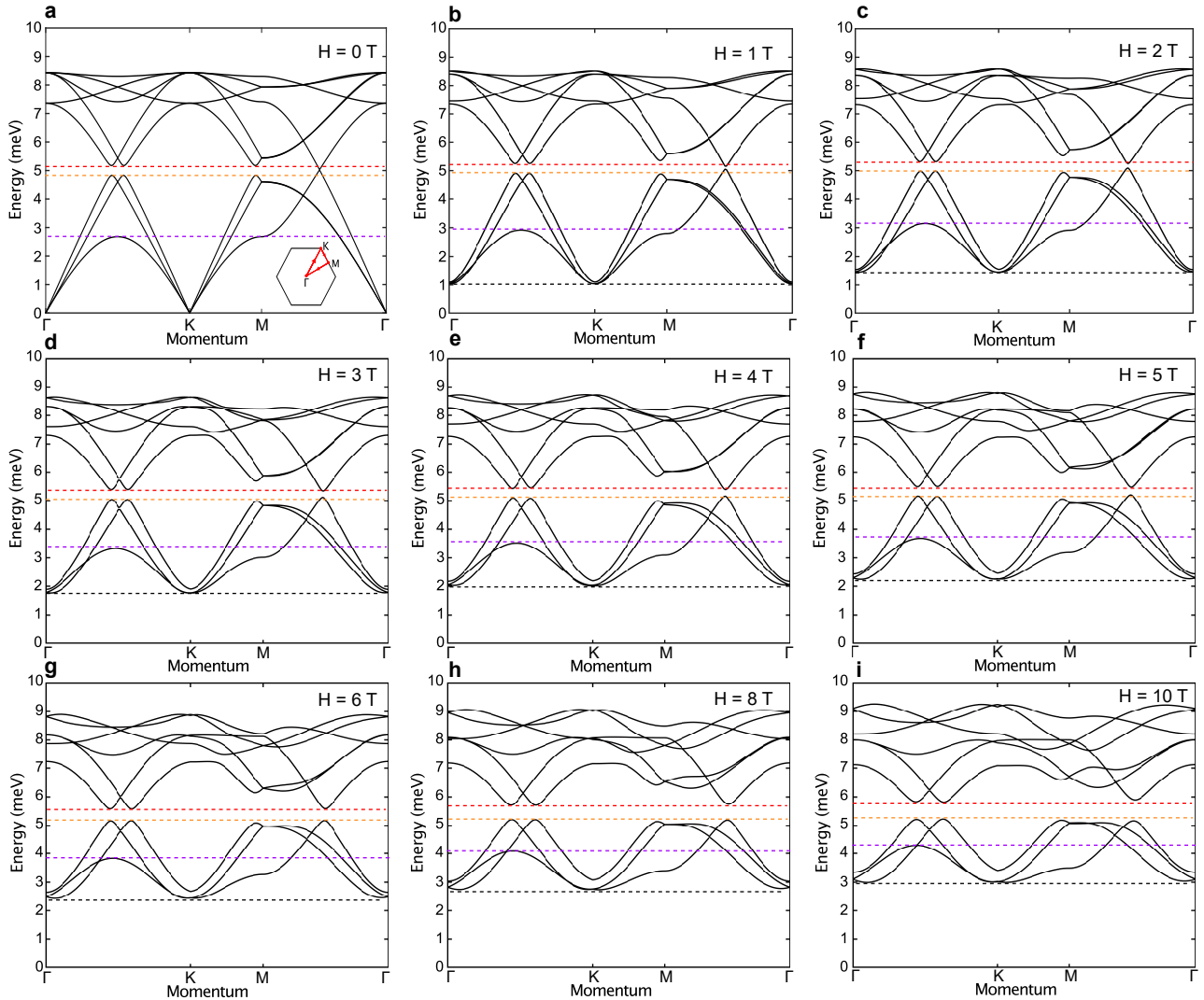


**Figure S12.** LSWT calculations with magnetic field. a-i) Dispersion in the first Brillouin zone (see inset of (a) for calculated path) with selected magnetic fields. Characteristic energy scales, discussed in the main text, are highlighted by colored dashed lines. Black dashed line: Minima of the  $\Gamma$  and  $K$  points.

The corresponding SDOS is shown in **Figure S13**. Here, the shifting of the weight to higher energies for increased magnetic field is evident. In addition to the discussion in the main text, we discuss the changes at the higher energies (between 6 and 10 meV). At  $H = 0$  the SDOS shows a sharp peak at around 8.3 meV. Under magnetic field the peak gets suppressed and its weight gets distributed over a larger energy range leading to an increase of the SDOS at around 6.8 meV /  $55 \text{ cm}^{-1}$ , i.e. the range of the lowest phonon tail. This field evolution might explain the shift of the phonon tail under magnetic field to lower energies, as observed in the magneto-THz experiment (main text).

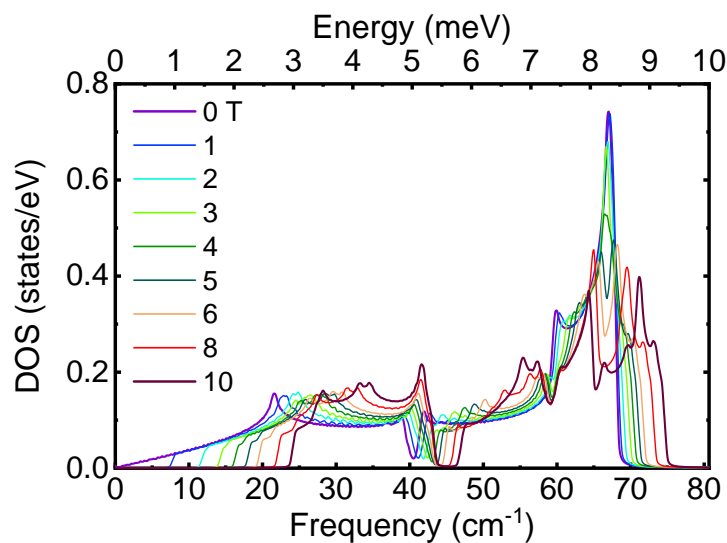


**Figure S13.** SDOS with magnetic field. Under magnetic field the SDOS becomes gapped and weight shifts to higher energies. Furthermore, between 6 and 10 meV, the weight gets distributed over a wider energy range.



## 16 Two-center magnon and three-center magnon excitation

For multi-center magnon absorption, i.e. the simultaneous flip of multiple spins by one photon, possible absorption can be either two-center or three-center magnon excitations. For each case, we consider the spin selection rule for linearly polarized THz light ( $\Delta S = 0$ <sup>[33,34]</sup>) in the magnetic ground state of Y-kapellasite. The two-center magnon excites two magnons simultaneously (left panel of **Figure S14**). Two scenarios are considered: two magnon excitations in one hexagon or two magnon excitations in different hexagons. Within a single hexagon, the  $\Delta S = 0$  selection rule is satisfied if two spins of opposite sign are flipped simultaneously. However, excitations comprising two different hexagons are forbidden. Here, the non-collinearity of the magnetic ground state results in  $\Delta S = \pm 1$ . For the three-center magnon, the situation is reversed (right panel of Figure S14). Three spin flips inside a single hexagon cannot satisfy the selection rule but result in spin momentum changes of higher order. However, if one spins in each of the three different hexagons is flipped, the net spin momentum does not change. Therefore, for linearly polarized light the spin selection rule allows two cases: two-center magnon in one hexagon or three-center magnon that involves three different hexagons. Between these two, flipping one spin in each hexagon (three-center magnon) seems to be energetically more favorable. Our high-field magnetization experiment supports this idea by showing a 1/6 plateau. Hence, three-center magnon, involving one spin-flip in each of the three different hexagon, is most likely the main contribution of the THz absorption. In order to fully exclude contributions from the spin-allowed two-center process, complete theoretical considerations of the involved selection rules are necessary. This remains the focus of a future study.

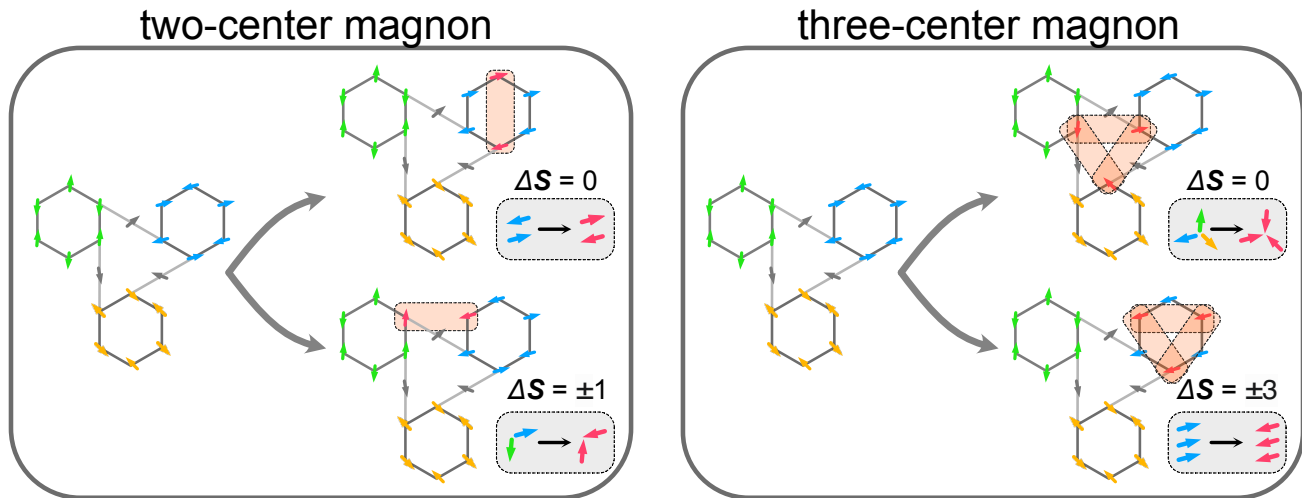


**Figure S14.** Possible multi-center magnon absorptions: two-center and three-center magnon in Y-kapellasite. Left panel: two-center magnon (red-shaded area) involving the simultaneous creation of two magnons (spin flips, grey-shaded inset) in one hexagon with  $\Delta S = 0$  or a creation of two magnons in two different hexagons,  $\Delta S = \pm 1$ . Right panel: three-center magnon. Here, the creation of three magnons in three different hexagons gives  $\Delta S = 0$ , whereas three magnons in the same hexagons yield  $\Delta S = \pm 3$ . Note that for the  $\Delta S = \pm 1$  /  $\Delta S = \pm 3$  cases only one of the two possible spin-flip pictures is sketched.

## 17 Comparison with Herbertsmithite

THz-TDS was carried out on Herbertsmithite ( $\text{ZnCu}_3(\text{OH})_6\text{Cl}_2$ ). The transmitted time-domain electric fields ( $\mathbf{E}_{\text{THz}} \parallel (a, b)$ ) are displayed in **Figure S15a**. Figure S15b shows corresponding absorption coefficient  $\alpha$ . The integrated absorption coefficient  $IA$  is shown in Figure S15c. At room temperature, the absorption coefficient is dominated by the tail of the lowest in-plane phonon mode (around  $85 \text{ cm}^{-1}$ <sup>[12]</sup>). Upon cooling the phonon shifts to higher energies, leading to a decrease of the  $IA$ . However, below  $T = 50 \text{ K}$ , the  $IA$  slightly increases again, similar to the previous report.<sup>[35]</sup> At low frequencies, we observe a monotonic response. As well, pronounced extended-time oscillations of the electric field are absent (Figure S15a). These observations are in stark contrast to the measurements on Y-kapellasite (see main text). Overall, our THz setup successfully reproduced the previous results on Herbertsmithite (Reference<sup>[35]</sup>), supporting that all differences between Y-kapellasite and Herbertsmithite THz spectra are due to the different magnetic ground states.

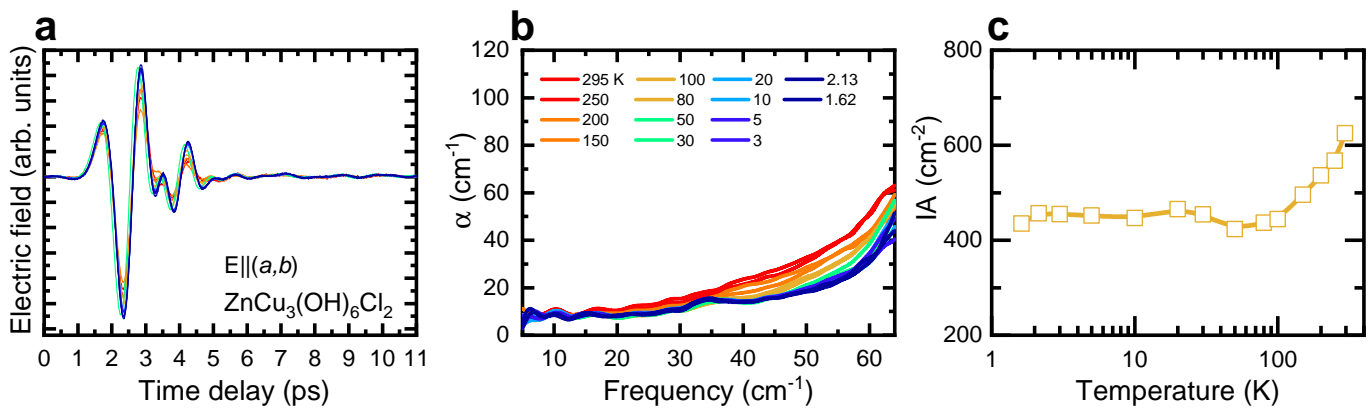


**Figure S15.** THz-TDS on  $\text{ZnCu}_3(\text{OH})_6\text{Cl}_2$ . a,b) Time domain electric field and absorption coefficient for the in-plane  $\mathbf{E} \parallel (a, b)$  response, respectively. c) Integrated absorption coefficient  $IA$  (up to  $46 \text{ cm}^{-1}$ ).

## References

- [S1] P. Puphal, M. Bolte, D. Sheptyakov, A. Pustogow, K. Kliemt, M. Dressel, M. Baenitz, C. Krellner, *J. Mater. Chem. C* **2017**, *5* 2629.
- [S2] Q. Barthélemy, P. Puphal, K. M. Zoch, C. Krellner, H. Luetkens, C. Baines, D. Sheptyakov, E. Kermarrec, P. Mendels, F. Bert, *Phys. Rev. Mater.* **2019**, *3* 074401.
- [S3] W. Sun, T. Arh, M. Gomilšek, P. Koželj, S. Vrtnik, M. Herak, J.-X. Mi, A. Zorko, *Phys. Rev. Mater.* **2021**, *5* 064401.
- [S4] W. Sun, Y.-X. Huang, S. Nokhrin, Y. Pan, J.-X. Mi, *J. Mater. Chem. C* **2016**, *4* 8772.
- [S5] R. T. Schumacher, C. P. Slichter, *Phys. Rev.* **1956**, *101* 58.
- [S6] Y. Skourski, M. D. Kuz'min, K. P. Skokov, A. V. Andreev, J. Wosnitza, *Phys. Rev. B* **2011**, *83* 214420.
- [S7] Y. Kohama, H. Ishikawa, A. Matsuo, K. Kindo, N. Shannon, Z. Hiroi, *Proc. Natl. Acad. Sci. U.S.A.* **2019**, *116*, 22 10686.
- [S8] O. Janson, S. Furukawa, T. Momoi, P. Sindzingre, J. Richter, K. Held, *Phys. Rev. Lett.* **2016**, *117* 037206.
- [S9] C. C. Homes, M. Reedyk, D. A. Cradles, T. Timusk, *Appl. Opt.* **1993**, *32*, 16 2976.
- [S10] M. Dressel, A. Pustogow, *J. Phys. Condens. Matter* **2018**, *30*, 20 203001.
- [S11] D. B. Tanner, *Optical Effects in Solids*, Cambridge University Press, Cambridge, **2019**.
- [S12] Y. Li, A. Pustogow, M. Bories, P. Puphal, C. Krellner, M. Dressel, R. Valentí, *Phys. Rev. B* **2020**, *101* 161115.
- [S13] I. I. Mazin, *Phys. Rev. B* **2010**, *81* 140508.
- [S14] R. D. Johnson, I. Broeders, K. Mehlawat, Y. Li, Y. Singh, R. Valentí, R. Coldea, *Phys. Rev. B* **2019**, *100* 214113.
- [S15] A. Togo, F. Oba, I. Tanaka, *Phys. Rev. B* **2008**, *78* 134106.
- [S16] A. Togo, I. Tanaka, *Scr. Mater.* **2015**, *108* 1.
- [S17] K. Parlinski, Z. Q. Li, Y. Kawazoe, *Phys. Rev. Lett.* **1997**, *78* 4063.
- [S18] J. P. Perdew, K. Burke, M. Ernzerhof, *Phys. Rev. Lett.* **1996**, *77* 3865.
- [S19] G. Kresse, J. Hafner, *Phys. Rev. B* **1993**, *47* 558.
- [S20] G. Kresse, J. Furthmüller, *Phys. Rev. B* **1996**, *54* 11169.
- [S21] G. Kresse, J. Furthmüller, *Comput. Mater. Sci.* **1996**, *6*, 1 15.
- [S22] K. Kozuki, T. Nagashima, M. Hangyo, *Opt. Express* **2011**, *19*, 25 24950.

- [S23] L. Pan, N. J. Laurita, K. A. Ross, B. D. Gaulin, N. P. Armitage, *Nat. Phys.* **2016**, *12*, 4 361.
- [S24] X. Zhang, F. Mahmood, M. Daum, Z. Dun, J. A. M. Paddison, N. J. Laurita, T. Hong, H. Zhou, N. P. Armitage, M. Mourigal, *Phys. Rev. X* **2018**, *8* 031001.
- [S25] N. J. Laurita, J. Deisenhofer, L. Pan, C. M. Morris, M. Schmidt, M. Johnsson, V. Tsurkan, A. Loidl, N. P. Armitage, *Phys. Rev. Lett.* **2015**, *114* 207201.
- [S26] N. J. Laurita, G. G. Marcus, B. A. Trump, J. Kindervater, M. B. Stone, T. M. McQueen, C. L. Broholm, N. P. Armitage, *Phys. Rev. B* **2017**, *95* 235155.
- [S27] P. Chauhan, F. Mahmood, H. J. Changlani, S. M. Koochpayeh, N. P. Armitage, *Phys. Rev. Lett.* **2020**, *124*, 3 037203.
- [S28] M. Dressel, G. Grüner, *Electrodynamics of Solids: Optical Properties of Electrons in Matter*, Cambridge University Press, Cambridge, **2002**.
- [S29] U. S. Pracht, E. Heintze, C. Clauss, D. Hafner, R. Bek, D. Werner, S. Gelhorn, M. Scheffler, M. Dressel, D. Sherman, B. Gorshunov, K. S. Il'in, D. Henrich, M. Siegel, *IEEE Trans. Terahertz Sci. Technol.* **2013**, *3*, 3 269.
- [S30] S. Toth, B. Lake, *J. Phys. Condens. Matter* **2015**, *27*, 16 166002.
- [S31] M. Hering, F. Ferrari, A. Razpopov, I. I. Mazin, R. Valentí, H. O. Jeschke, J. Reuther, *Npj Comput. Mater.* **2022**, *8*, 1 10.
- [S32] R. S. Fishman, J. A. Fernandez-Baca, T. Rõõm, *Spin-Wave Theory and its Applications to Neutron Scattering and THz Spectroscopy*, Morgan & Claypool Publishers, San Rafael, **2018**.
- [S33] C. Cohen-Tannoudji, B. Diu, F. Laloë, *Quantum Mechanics VOL 2 2ed*, Wiley, New York, **2019**.
- [S34] C. Cohen-Tannoudji, B. Diu, F. Laloë, *Quantum Mechanics VOL 3 2ed*, Wiley, New York, **2020**.
- [S35] D. V. Pilon, C. H. Lui, T.-H. Han, D. Shrekenhamer, A. J. Frenzel, W. J. Padilla, Y. S. Lee, N. Gedik, *Phys. Rev. Lett.* **2013**, *111* 127401.